Center for Computational Engineering Science Mathematics Division

RWTH AACHEN UNIVERSITY

Diese Arbeit wurde vorgelegt am
Lehrstuhl für Mathematik (MathCCES)

Entwicklung eines Modells zur technisch-wirtschaftlichen Analyse von Solarturmkraftwerken

Development of a techno-economic model for solar tower power plants

Masterarbeit
Computational Engineering Science

November 2017

Vorgelegt von Presented by	Gregor Heiming gregor.heiming@rwth-aachen.de
Erstprüfer First examiner	Prof. Dr. Martin Frank Lehrstuhl für Mathematik (MathCCES) RWTH Aachen University
Zweitprüfer Second examiner	Prof. Alexander Mitsos, Ph.D. Lehrstuhl für Systemverfahrenstechnik (AVT.SVT) RWTH Aachen University
Koreferent Co-supervisor	Dr. rer. nat. Pascal Richter Lehrstuhl für Mathematik (MathCCES) RWTH Aachen University

Abstract

In this thesis, a techno-economic model for use in solar tower power plant design optimization is developed. It is comprised of models for the subsystems heliostat field, thermal receiver, thermal energy storage, power block, and a model for economic analysis. Each of the sub-models can be used separately. The sub-models are based on existing models from literature using simplified correlations. Special attention is paid to the efficiency while keeping reliable results. The developed code is an advancement for the SunFlower software.

Zusammenfassung

Es wird ein Modell zur technisch-wirtschaftlichen Analyse von Solarturmkraftwerken entwickelt, das in der Optimierung der Kraftwerksauslegung verwendet werden soll. Es besteht aus Teilmodellen für Heliostatenfeld, Receiver, Wärmespeicher, Kraftwerksblock, sowie einem Modell für die wirtschaftliche Auswertung des Kraftwerks. Für die Teilmodelle werden Ansätze aus der Literatur mit vereinfachten Modellgleichungen verwendet. Besonderes Augenmerk wird auf die Effizienz bei gleichzeitiger Erhaltung verlässlicher Ergebnisse gelegt. Das Modell ist als Erweiterung der SunFlower Software implementiert.

Contents

Nomenclature

Symbols

c	Specific cost	$[\$\mathrm{m}^{-2}]$
Gr	Grashof number	[–]
I	Investment cost	[$]
Nu	Nusselt number	[–]
pi	Price index	[–]
Pr	Prandtl number	[–]
pr	Progress ratio	[–]
$\dot{Q}$	Global heat flow	$[\mathrm{Wm}^{-2}]$
$\dot{q}$	Local heat flow	$[\mathrm{Wm}^{-2}]$
Re	Reynolds number	[–]
η	Efficiency	[%]
σ	Stefan-Boltzmann constant $\sigma = 5.67 \cdot 10^{-8}$	$[\mathrm{Wm}^{-2}\,\mathrm{K}^{-4}]$

Subscripts

amb	Ambient
$conv$	Convection
htf	Heat transfer fluid
inc	Incident
pcu	Power conversion unit/Power block
rad	Radiation
rec	Receiver
ref	Reflection or Reference

Acronyms

AEP	Annual energy production
CAPEX	Capital expenditure
CFD	Computational fluid dynamics
CSP	Concentrated solar power
DNI	Direct normal irradiation
HTF	Heat transfer fluid
IRR	Internal rate of return
LCOE	Levelized cost of electricity
LEC	Leveleized energy cost
NPV	Net present value
O&M	Operations and maintenance
OPEX	Operational expenditure
PCU	Power conversion unit
PV	Photovoltaics
SAM	System Advisor Model
TES	Thermal energy storage
ToE	Tariff of electricity

List of Figures

List of Tables

1 Introduction

Energy production using concentrated solar power (CSP) is one of the most promising concepts for covering the huge demand of electric energy of the future. The sun provides almost infinite power, so as a source of energy, it is not only sustainable but inexhaustible for the lifetime of human kind. Figure 1 shows the direct normal irradiation (DNI) distribution on the Earth's surface.

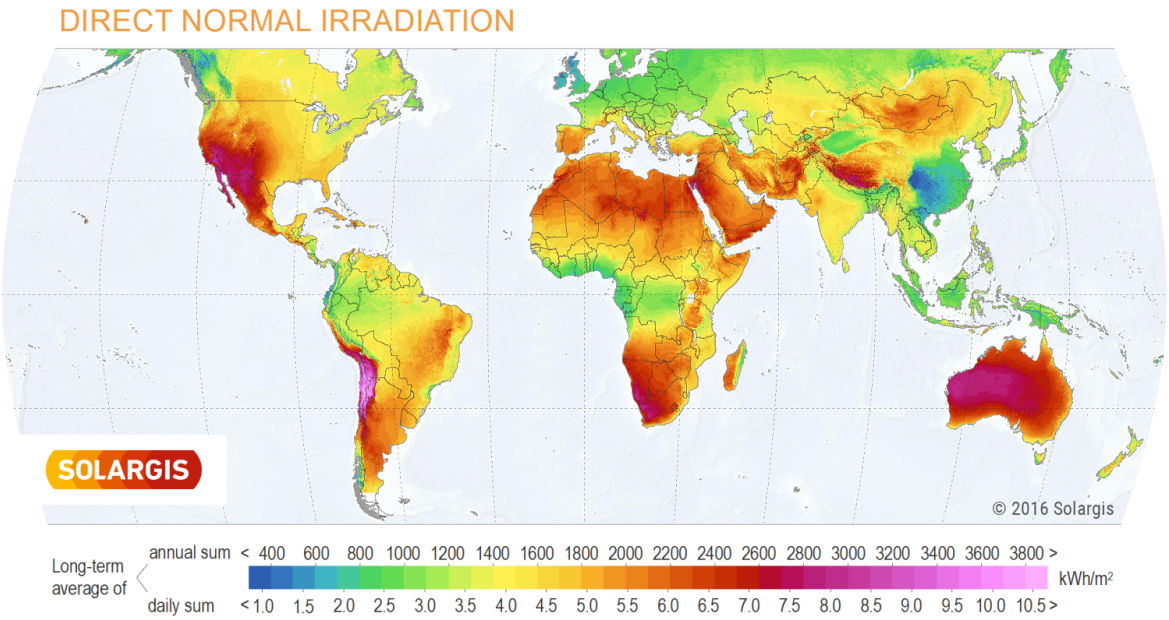

Figure 1: Direct normal irradiation (DNI) World Map [60].

The idea behind CSP is the efficient conversion of solar radiation into thermal energy by focusing and, thereby, obtaining very high temperatures. Focusing can be performed by lenses or by mirrors. However, due to their broader applicability and better scalability, mirrors are usually preferred. These mirrors track the sun so that their reflection always hits the absorber. Since CSP systems convert radiation into heat, the power can be dispatched by installing a thermal storage. As heat can better be stored than electricity, this is a significant advantage of CSP compared to other renewable energy systems.

The area of concentrated solar power can be divided into two basic approaches: Line-focusing and point-focusing systems.

Line-focusing systems are namely parabolic trough (Figure 2b) or linear Fresnel collectors (Figure 2a) with one single tracking axis. Here, the radiation is focused on an absorber tube where some heat transfer fluid (HTF) absorbs the incident power.

Examples for point-focusing systems are the solar dish, a single construction including the reflecting mirror and an absorber (Figure 2c), and solar tower systems, also called central receiver system (Figure 2d). Here, reflector and absorber are separated. The reflector is a large array of mirrors set up on a field around a central tower that

(a) Linear Fresnel collector [46]

(b) Parabolic Trough collector [23]

(c) Solar Dish [22]

(d) Solar Tower [23]

Figure 2: Examples of CSP Systems.

has the receiver on top. The reflectors of point-focusing systems track the sun with two axes.

We focus our work on solar tower systems. In comparison with the other previously described systems, solar towers can obtain higher temperatures than it is possible with line-focusing systems. Furthermore, solar towers are scalable: Power outputs in the magnitude of 100 kW (Helio100, South Africa) and 370 MW (Ivanpah, USA) can be reached. The components of a solar tower power plant are shown in Figure 3.

In this work, a techno-economic model for use in solar tower power plant design optimization is developed. Since this model needs to be evaluated frequently during an optimization process, it needs to be efficient while still resulting in reliable results. Different optimization approaches are discussed in Section 2.3.

In the following sections, models for the performance evaluation of solar tower power plants are presented. These are the heliostat field model in Section 2 computing the optical energy reaching the central receiver, a thermal receiver model in Section 3 converting the optical power into thermal power of a heat transfer fluid (HTF). Section 4 then describes the thermal storage system, followed by the description of the power block in Section 5 which corresponds to the power block of a conventional thermal power plant. In Section 6, a model for the economic evaluation of the plant is

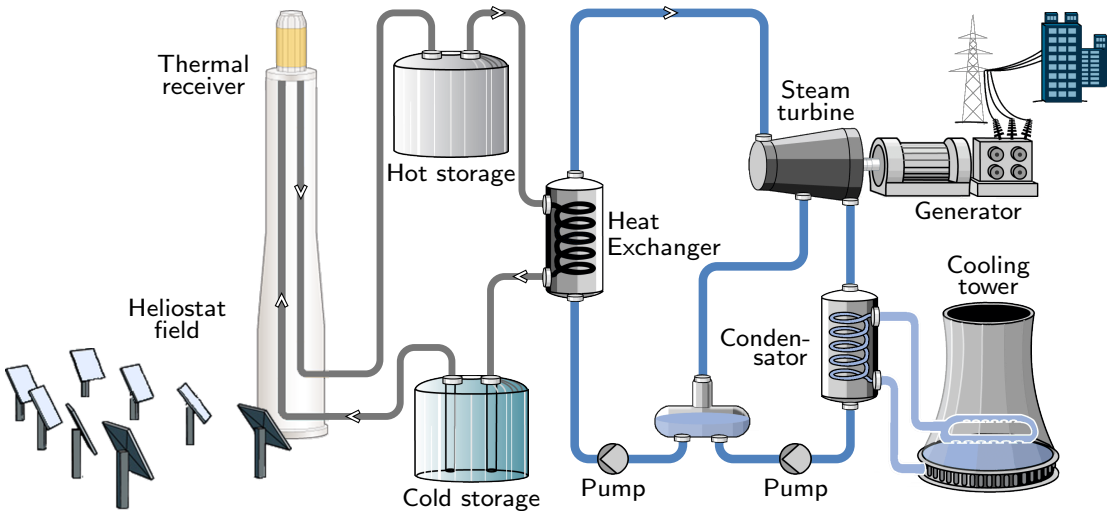

Figure 3: Overview of a solar tower power plant [48].

presented. The models are validated and discussed in Section 7.

The software developed in the course of this work is based on the ray tracer SunFlower [50] that is developed at the institution of the author.

2 Heliostat Field

The largest component of a solar tower power plant is the mirror field. Hundreds to thousands of sun-tracking mirrors, the so-called heliostats, are placed on a field. They collect the incoming solar radiation by aligning according to the current sun position. In this Section, the optical performance model of SunFlower will be described. Additionally, a new approach for the efficient ray generation on triangular heliostat facets is presented. When modeling the performance of the heliostat field, several loss factors need to be considered. These are discussed in Section 2.2. At the end of this Section, methods for optimizing the optical performance of heliostat fields will be discussed (→ 2.3).

2.1 Heliostat Geometry

Heliostats typically consist of several individual facets, the actual mirrors, that are mounted onto the heliostat scaffold. When aligning the heliostat with the sun, the facets stay fixed on the heliostat while the whole scaffold is rotated. Facets can be slightly tilted so that they form a curvature, the so-called canting. There is on-axis canting where the facets form the center of a symmetric paraboloid (the heliostat center is *on* the paraboloid *axis*), and off-axis canting where the facets describe a piece of a paraboloid that is *off* the paraboloid *axis* [see 48]. In addition to facet canting, the facets can also be curved with a given focal length.

Facets can be rectangular or triangular. This allows the simulation of most heliostat fields including those using the pentagonal Stellio Heliostat [6] that consists of ten triangular facets (see Figure 4b). Since typically rectangular facets are used, the use of triangular facets brings new challenges into the modeling and simulation of the heliostat field performance, see Section 2.2.4. As the Stellio heliostat seems to be very promising concerning its reduced blocking and shading effects [3], and its aiming quality [6], these challenges are undertaken in this work.

Usually, each heliostat has its own foundation. However, there are also approaches of clustering heliostats on a common pod (Figure 4d), so that the foundation costs are decreased [36]. Different types of heliostats are shown in Figure 4.

2.2 Optical Performance Computation

The efficiency of the heliostat field is defined as the fraction of the actual received radiation at the receiver over the incoming radiation that could possibly be collected by the heliostats, i.e., DNI × total mirror area. In the SunFlower simulation, the efficiency is broken up into several sub-efficiencies: Cosine, blocking, shading, spillage, reflectivity, and atmospheric attenuation. This can be expressed as

$$\overline{\eta}_{field} = \overline{\eta}_{cos} \cdot \overline{\eta}_{blocking} \cdot \overline{\eta}_{shading} \cdot \overline{\eta}_{spillage} \cdot \overline{\eta}_{ref} \cdot \overline{\eta}_{aa} \tag{2.1}$$

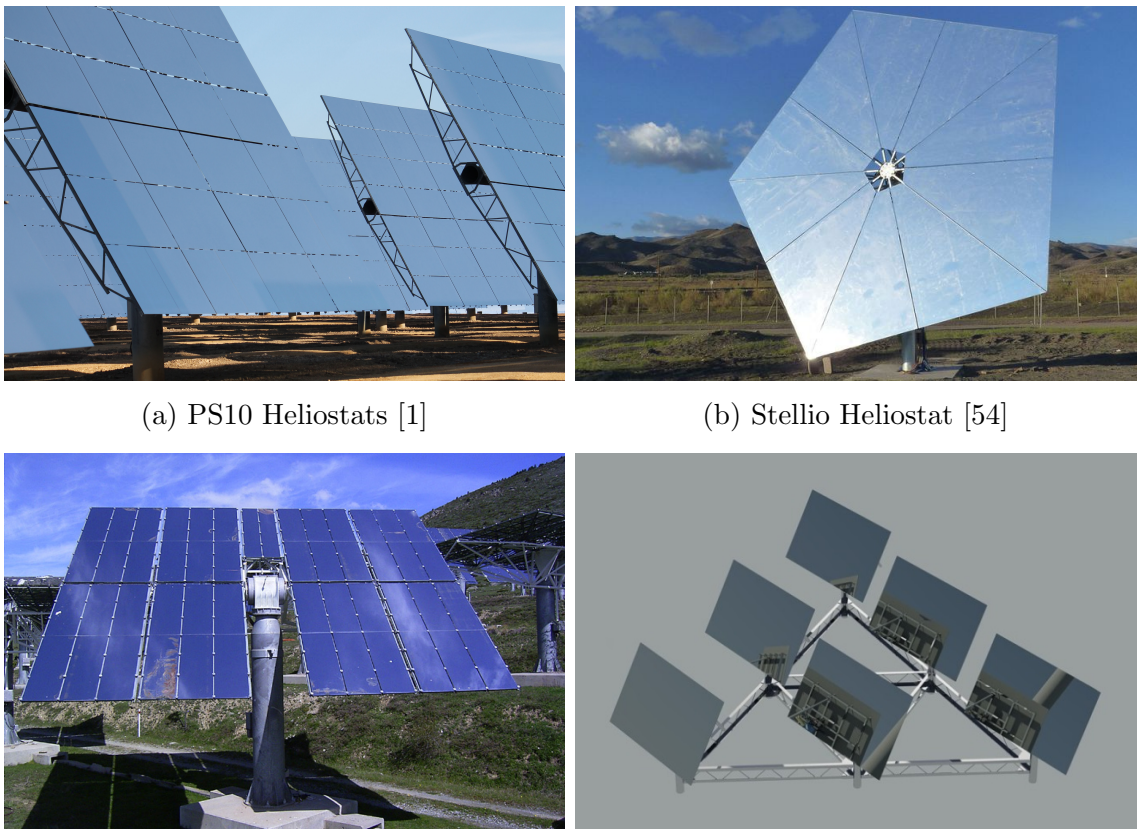

(a) PS10 Heliostats [1]

(b) Stellio Heliostat [54]

(c) THEMIS Heliostat [14]

(d) Helio100 Heliostat Pod [19]

Figure 4: Examples of heliostat geometries that can be modeled in SunFlower.

with averaged efficiencies

$$\overline{\eta} = \sum_{i=0}^{N_{heliostats}} \eta_i. \tag{2.2}$$

The optical efficiencies are described in [49] and will be reconstructed here, together with a description of how the loss evaluations are implemented in the SunFlower code. Shading, blocking and spillage require ray tracing and are, therefore, preceded by the subsection about ray generation.

2.2.1 Cosine Effect

When tracking the sun, the heliostats are never aligned directly towards the sun. Therefore, the effective area of the heliostat is reduced by the cosine of the angle α between heliostat normal $\boldsymbol{n}_i$ and sun direction vector $\boldsymbol{d}_{sun}$

$$\eta_{cos,i} = \boldsymbol{d}_{sun} \cdot \boldsymbol{n}_i = \cos(\alpha). \tag{2.3}$$

This optical loss is, hence, called cosine effect.

2.2.2 Reflectivity

Even the best mirrors can only reflect a fraction of the incident light. The reflectivity value is typically between 85 and 97 % and can depend on the incident angle [72]. Additionally, the reflectivity is decreased due to soiling of the mirror surface [45].

$$\eta_{ref,i} = \rho(\alpha) \cdot f_{soil}. \tag{2.4}$$

2.2.3 Atmospheric Attenuation

The attenuation due to the atmosphere is a function of the distance d_i between heliostat and receiver:

$$\eta_{aa,i} = \begin{cases} 0.993\,21 - 1.176 \cdot 10^{-4}\, d_i + 1.97 \cdot 10^{-8}\, d_i^2 & \text{for } d_i \leq 1000\,\text{m} \\ \exp\left(-1.106 \cdot 10^{-4}\, d_i\right) & \text{for } d_i > 1000\,\text{m} \end{cases} \tag{2.5}$$

The equation is taken from Schmitz et al. [55].

2.2.4 Ray Generation on Heliostat Facets

The ray tracing can be seen as an integration of the ray power over the facet area. Therefore, two-dimensional quadrature is used in SunFlower to generate rays on the facet surface. These rays are then grasped as representatives for a certain area of which the size is given by the quadrature weights.

Since for this work also triangular heliostat facets were implemented, a quadrature method for triangular domains is presented in this section.

Rectangular Heliostat Facets For the ray distribution on rectangular heliostat facets, the two-dimensional Gauss-Legendre quadrature rule is used, which has the advantage of a higher resolution near the facets' edges where most shading and blocking effects occur.

Quadrature in general is a numerical approximation of an integral by a sum of weighted function evaluations:

$$\int_a^b f(x)\,\mathrm{d}x \approx (b-a) \sum_{i=1}^{N} w_i f(x_i). \tag{2.6}$$

For Gaussian quadrature, the evaluation points x_i correspond to the roots of orthogonal polynomials. The Gaussian weights w_i are strictly positive which results in higher stability compared to other quadrature formulas [16]. The most common Gaussian quadrature is the Gauss-Legendre quadrature which is associated with Legendre polynomials. Gaussian quadrature rules of order N are exact for polynomials of degree up to $2N + 1$ [16].

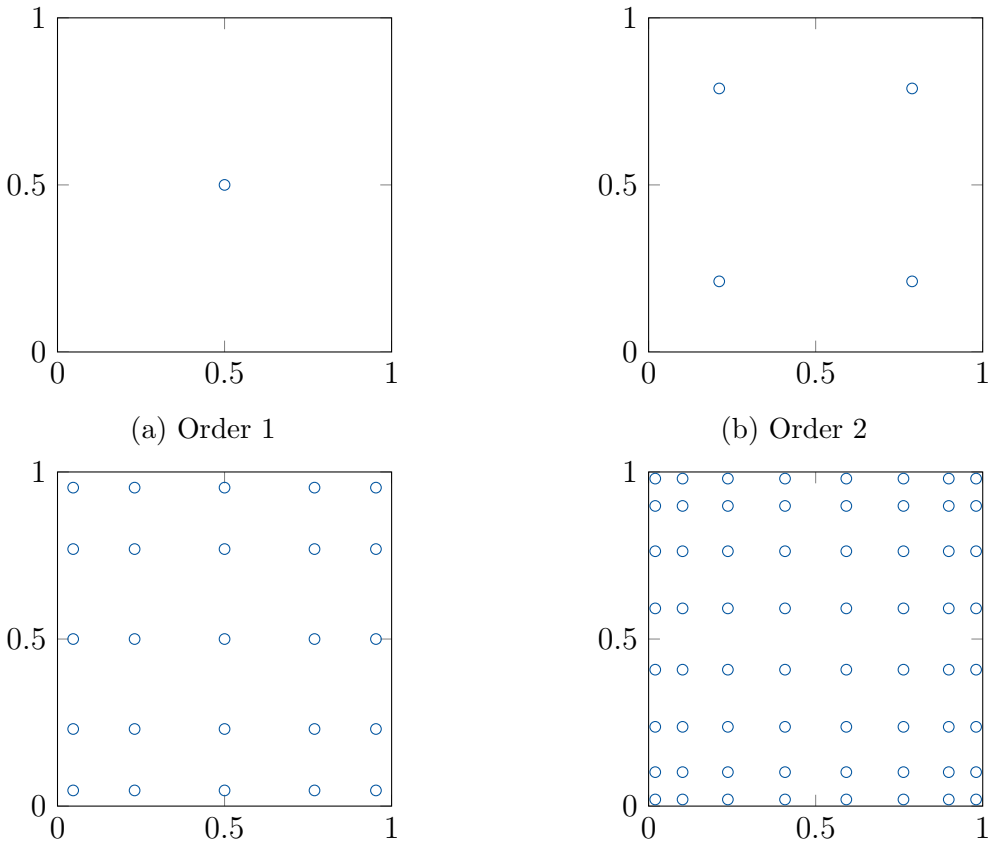

(a) Order 1

(b) Order 2

(c) Order 5

(d) Order 8

Figure 5: Gaussian quadrature points on the unit square.

A two-dimensional Gaussian quadrature rule can be created from two one-dimensional rules by simple chaining.

$$\begin{aligned}\int_{y_{\text{lb}}}^{y_{\text{ub}}}\int_{x_{\text{lb}}}^{x_{\text{ub}}} f(x,y)\,\mathrm{d}x\,\mathrm{d}y &\approx \int_{y_{\text{lb}}}^{y_{\text{ub}}} (x_{\text{ub}}-x_{\text{lb}})\sum_{i=1}^{N_x} w_i f(x_i,y)\,\mathrm{d}y \\ &= (x_{\text{ub}}-x_{\text{lb}})\sum_{i=1}^{N_x} w_i \int_{y_{\text{lb}}}^{y_{\text{ub}}} f(x_i,y)\,\mathrm{d}y \\ &\approx (x_{\text{ub}}-x_{\text{lb}})(y_{\text{ub}}-y_{\text{lb}})\sum_{i=1}^{N_x}\sum_{j=1}^{N_y} \underbrace{w_i\omega_j}_{\hat{w}_{i,j}} f(x_i,y_j)\end{aligned} \tag{2.7}$$

The points of 2D tensorized Gauss-Legendre quadrature rules of different orders are shown in Figure 5.

Triangular Heliostat Facets For triangular domains, the intuitively chained two-dimensional quadrature as shown in (2.7) cannot simply be applied. The points could

be transformed from a rectangular to a triangular domain, but as pointed out by Deng [17], a larger number of points is required for higher orders and the points are then distributed unsymmetrically.

Symmetrical quadrature formulas for triangles can be constructed, see e.g., [17, 21, 30, 39, 64, 67]. Here, we will discuss the approach of Dunavant [21] as it is the classical approach for triangular Gaussian quadrature. It is based on the idea of Lyness and Jespersen [39] applied to the unit triangle T_2 (Figure 6a) with

$$T_2 = \{(\xi, \eta) \mid 0 \leq \xi, \eta, \xi + \eta \leq 1\}. \tag{2.8}$$

A quadrature rule that is exact for polynomials of degree p shall be constructed, i.e.,

$$\int_{T_2} f(x,y)\,\mathrm{d}x\,\mathrm{d}y \overset{!}{=} \underbrace{|T_2|}_{=\frac{1}{2}} \sum_{i=1}^{N} w_i f(x_i, y_i) \quad \text{for all} \quad f(x,y) \in \boldsymbol{P}_p(x,y) \tag{2.9}$$

with

$$\boldsymbol{P}_p(\xi,\eta) = \operatorname{span}\left\{\xi^i \eta^j \mid 0 \leq i, j, i+j \leq p\right\}. \tag{2.10}$$

Substituting the polynomial definition into Equation (2.9) and applying the identity (2.11) as given by Stroud and Secrest [64],

$$\int_{T_2} x^i y^j \,\mathrm{d}x\,\mathrm{d}y = \frac{i!\,j!}{(i+j+2)!} \tag{2.11}$$

we can set up a system of nonlinear moment equations from the basis of $\boldsymbol{P}_p(x,y)$:

$$1: \qquad \frac{1}{2} = \frac{1}{2}\sum_{i=0}^{N} w_i \tag{2.12a}$$

$$x: \qquad \frac{1}{6} = \frac{1}{2}\sum_{i=0}^{N} w_i x_i \tag{2.12b}$$

$$y: \qquad \frac{1}{6} = \frac{1}{2}\sum_{i=0}^{N} w_i y_i \tag{2.12c}$$

$$x^2: \qquad \frac{1}{12} = \frac{1}{2}\sum_{i=0}^{N} w_i x_i^2 \tag{2.12d}$$

$$xy: \qquad \frac{1}{24} = \frac{1}{2}\sum_{i=0}^{N} w_i x_i y_i \tag{2.12e}$$

$$y^2: \qquad \frac{1}{12} = \frac{1}{2}\sum_{i=0}^{N} w_i y_i^2 \tag{2.12f}$$

$$\vdots$$

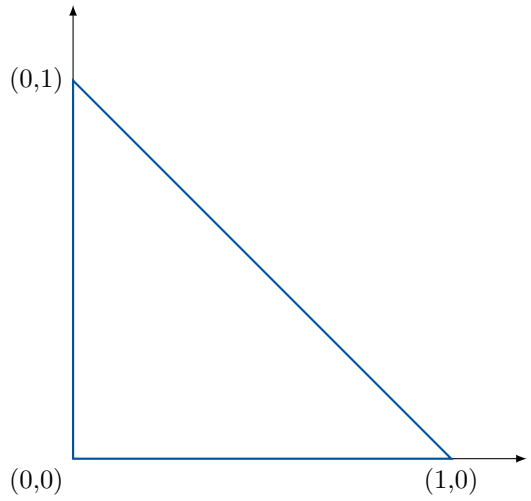

(a) Unit Triangle T_2

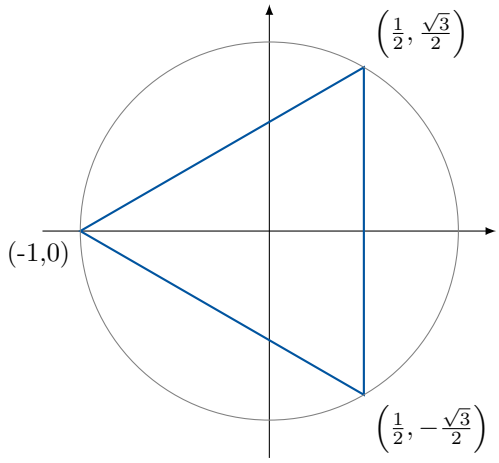

(b) Equilateral triangle $\triangleleft$ as used in Dunavant [21], and Lyness and Jespersen [39]

Figure 6: Triangles on the base of which the symmetrical triangle quadrature rules are developed.

For a first order quadrature method ($p = 1$), only Equations (2.12a) to (2.12c) are relevant. The solution of the (sub-)system is then obviously given with $N = 1$ and

$$w_1 = 1, \quad x_1 = y_1 = \frac{1}{3},$$

see Figure 7a.

For a second order method, Equations (2.12a) to (2.12f) need to be considered. For orders $p \geq 2$, the system of equations is not independent and, thus, hard to solve. Dunavant [21] provides an equation for the number of independent equations m:

$$m = \frac{(p+3)^2 + \alpha_p}{12} \tag{2.13}$$

where

$$\alpha_p = \begin{cases} 3 & p = 0 \\ -4 & p \in \{1, 5\} \\ -1 & p \in \{2, 4\} \\ 0 & p = 3 \\ \alpha_{p-6} & p \geq 6 \end{cases} \tag{2.14}$$

Instead of reducing the system of equations (2.12), Dunavant [21] as well as Lyness and Jespersen [39] propose working on an equilateral triangle $\triangleleft$ which has the unit circle as its circumcircle, see Figure 6b. The problem is then solved in polar coordinates (r, θ) with

$$x = r\,\cos(\theta) \quad \text{and} \quad y = r\,\sin(\theta)$$

and makes use of the symmetry of the triangle. This approach has the advantage of directly resulting in a system of m independent moment equations. The method of Lyness and Jespersen [39] will be briefly reproduced in the following.

Writing the monomial $x^i y^j$ with $i + j = q$ in polar coordinates gives

$$\begin{aligned} x^i y^j = x^{q-j} y^j &= r^q \cos(\theta)^{q-j} \sin(\theta)^j \\ &= r^q \left(\frac{e^{\mathrm{i}\theta} + e^{-\mathrm{i}\theta}}{2} \right)^{q-j} \left(\frac{e^{\mathrm{i}\theta} - e^{-\mathrm{i}\theta}}{2\mathrm{i}} \right)^j \\ &= \frac{r^q}{2^q} \frac{1}{\mathrm{i}^j} \left(e^{\mathrm{i}\theta} + e^{-\mathrm{i}\theta} \right)^{q-j} \left(e^{\mathrm{i}\theta} - e^{-\mathrm{i}\theta} \right)^j, \end{aligned} \tag{2.15}$$

a linear combination of the polynomials

$$r^q e^{p\mathrm{i}\theta} \quad \text{with} \quad p = -q, -q+2, -q+4, \ldots, q-2, q. \tag{2.16}$$

A set of polar moment equations

$$\nu_{q,p} = \frac{1}{A} \int_{\triangleleft} w(r, \theta)\, r^q e^{p\mathrm{i}\theta}\, r \,\mathrm{d}r \,\mathrm{d}\theta \tag{2.17}$$

is set up according to the system (2.12) with

$$A = \int_{\triangleleft} w(r, \theta)\, r \,\mathrm{d}r \,\mathrm{d}\theta \,. \tag{2.18}$$

Using the triangle symmetry in the system of moment equations, a set of m independent nonlinear equations can be obtained. Since solving systems of nonlinear equations is fairly costly and results strongly depend on the initial guess, the method was not implemented during this work. Instead, an open source library was integrated [10]. The points of triangular Dunavant Gauss quadrature rules on the unit triangle T_2 are shown in Figure 7 for different orders.

Now, the ray generation points on the facets can be computed so we can look at the optical loss factors of a heliostat field that requires ray tracing.

2.2.5 Shading and Blocking

The effect of an object (e.g., heliostat or tower) standing between a heliostat and the sun is called shading. A heliostat can be fully shaded or by an arbitrary fraction. If the sunlight reflected by the heliostat doesn't reach the receiver because of another heliostat standing in-between, this is called blocking. See Figure 8 for clarification.

For an efficient computation of the blocking (shading) efficiencies, a hierarchical approach is used [7, 50]. As a first step, the possibly blocking (shading) heliostats are preselected using a bitboard-like data structure (Figure 9). In a second step, the three-dimensional distance between the path of the light and the possibly blocking (shading) heliostats is checked so that further heliostats can be dropped from the

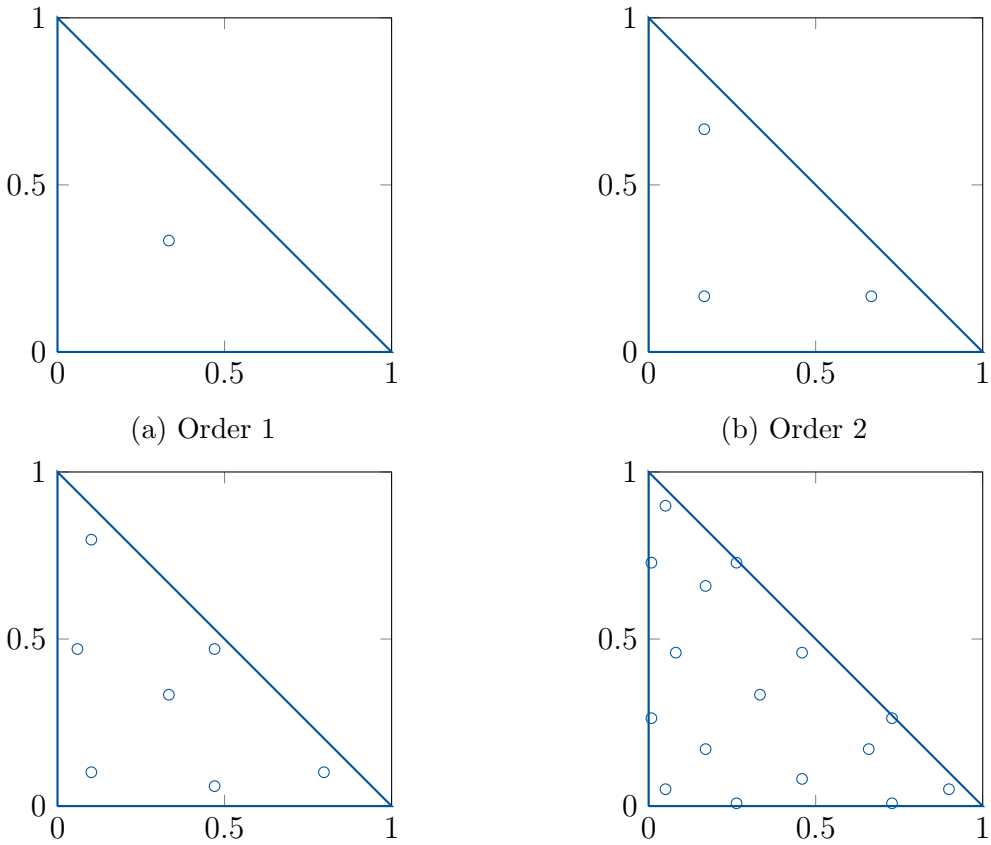

(a) Order 1

(b) Order 2

(c) Order 5

(d) Order 8

Figure 7: Gaussian quadrature points on the unit triangle.

preselection. The same is done for each facet before the actual blocking (shading) fraction is evaluated by ray tracing. The steps are visualized in Figure 10. Since the efficiencies of blocking and shading are obtained by ray tracing, there is no explicit formula given for $\eta_{blocking,i}$ and $\eta_{shading,i}$.

2.2.6 Spillage

The spillage loss $(1 - \eta_{spillage,i})$ is the part of the reflected radiation that doesn't hit the receiver. In the computation of these losses, the optical errors and uncertainties need to be considered: These are the sun shape, the tracking errors of both heliostat rotation axes, the slope error. In SunFlower, these errors are combined to one single cumulative error distribution.

The optical simulation of the heliostat field in the SunFlower software has four different approaches implemented which are further described in Richter et al. [50]. Here is a short summary:

Figure 8: Blocking effects in the Crescent Dunes Plant, Nevada (USA) [61].

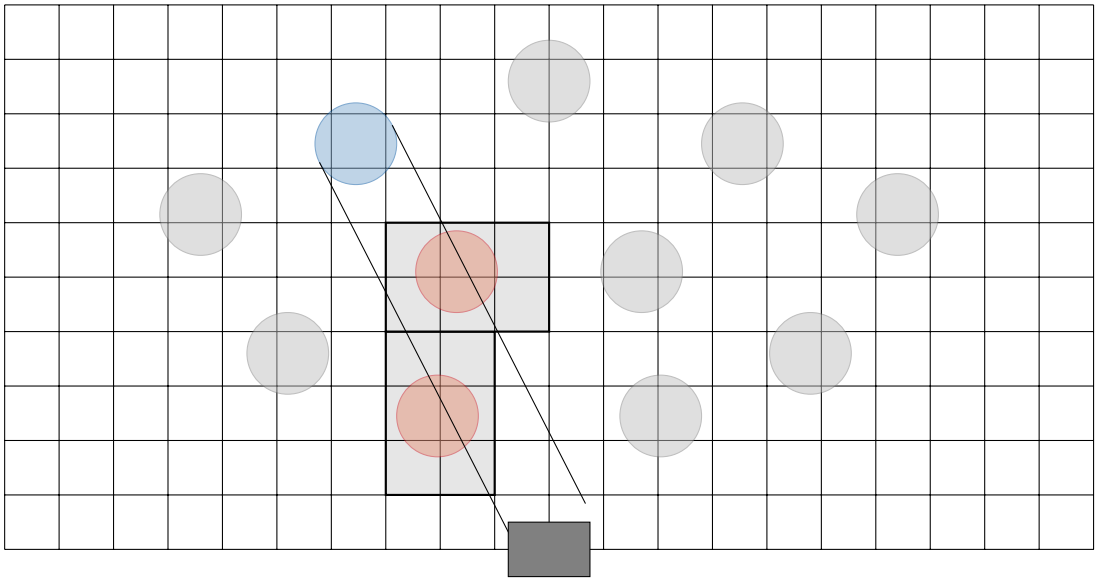

Figure 9: Bitboard-like structure for fast shading and blocking preselection [cf. 48].

Monte-Carlo ray tracing The idea of Monte-Carlo ray tracing is using large bulks of rays with some randomized perturbations according to the optical errors. This means that this approach is only exact for very large numbers of rays and a significant drawback is its indeterminism. Monte-Carlo ray tracing is used by most optical simulation software, e.g., SolTrace [69, 70] or Tonatiuh [8, 11], as it is applicable to any geometry. SolTrace additionally uses a randomized ray distribution on the heliostat facets. The Monte-Carlo method converges with a rate of $\frac{1}{2}$ [27].

Quasi-Monte-Carlo Method With the Quasi-Monte-Carlo approach the number of required rays can be decreased compared to the classical Monte-Carlo ray tracing. Here, a certain number of ray generation points is chosen and at each of these positions several differently perturbed rays are generated pseudo-randomly using a Sobol

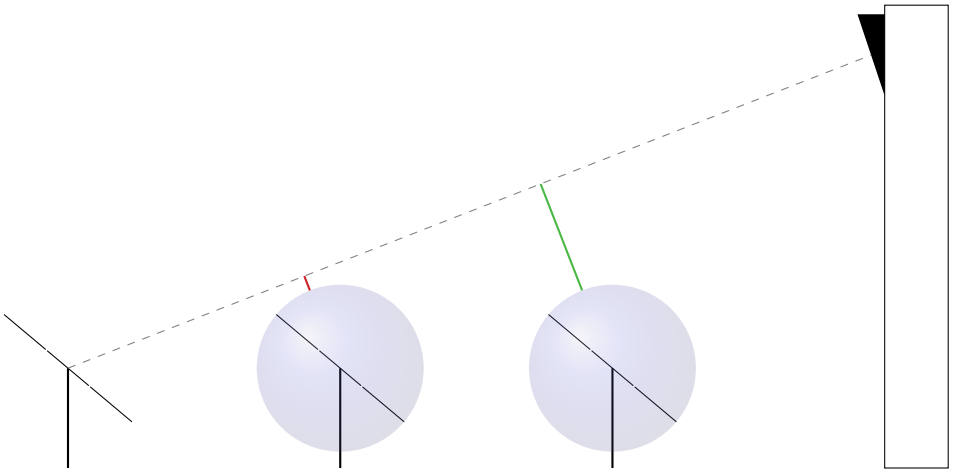

(a) Check Heliostat

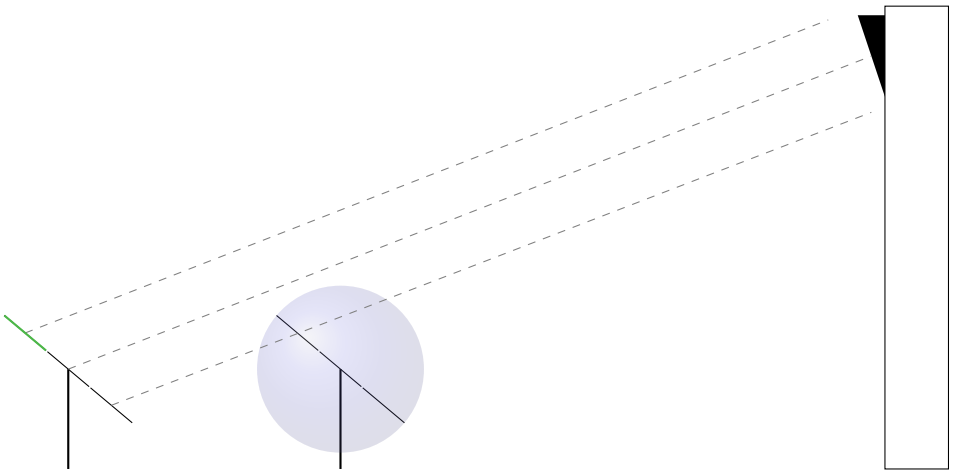

(b) Check Facets

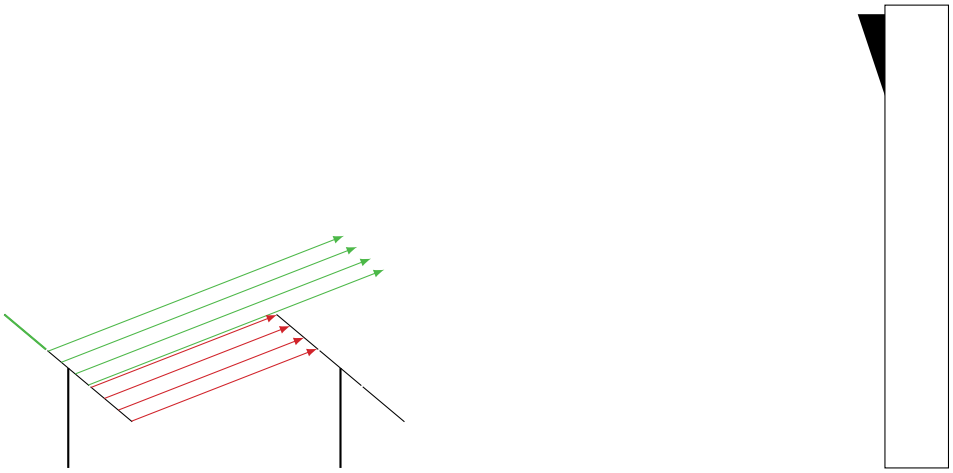

(c) Ray Tracing

Figure 10: Visualization of the hierarchical blocking computation [31].

sequence. The convergence rate can be improved to almost 1 [27].

Convolution Method With this approach, even fewer rays are generated where each ray is a representative for a certain area of the heliostat facet. Optical errors are taken into account analytically. This allows a much faster computation of the received optical power due to the heavily reduced number of traced rays. This method is an advancement of the method presented by Noone et al. [42].

Area Convolution The heliostat facets are divided into several areas that are assumed to be locally flat. Using convolution, these locally flat areas can be projected onto the receiver surface so that the receiver power can be computed analytically exact. [31, 50]

2.3 Heliostat Field Optimization Strategies

Due to its size and complexity, the heliostat field offers several different approaches of optimizing the costs and the optical performance. In this short summary, we will skip the single heliostat design optimization that reduces optical tracking errors or the heliostat production costs. Instead, the focus will be on the overall heliostat field. Here, the largest area is the heliostat field layout optimization. The aim is the minimization of cosine, shading and blocking losses with considering the feasibility and practicability. The different field layout optimization approaches can roughly be categorized into field growth methods, pattern-based methods, and free variable methods.

In field growth methods, the heliostats are added one by one at optimal positions with considering (but without changing) the previously added heliostats. This method can't be parallelized because the heliostat positioning in each step highly depends on the preceding steps. However, field growth methods can be used if the desired power is provided instead of the desired number of heliostats as the algorithm can terminate as soon as the desired power output is reached. Implementations of this method are, e.g., given by [18, 52].

Pattern-based methods only allow feasible field layouts. A predefined pattern is optimized using few parameters compared to each separate position. This makes the pattern-based approach relatively fast. Due to its strong restriction, this method will never obtain a better result than an optimization of each heliostat's position. On the other hand, it can easily be parallelized and the result is usually directly feasible. The most common pattern is the radially staggered grid, see Figures 11a to 11d. Noone et al. [42] propose using a biomimetic layout. Other pattern are possible, e.g., rows (see Figure 11e) or hexagonal patterns [3].

Free variable methods optimize all heliostat positions at the same time. This makes finding a global optimum possible (though very unlikely). Since the parameter space is huge with two parameters per heliostat and hundreds to thousands of heliostats, typically heuristic methods are used, e.g., genetic/evolutionary algorithms [49]. For a local search, e.g., as a post-processing step or in multi-step optimization approaches, gradient based methods are used [38].

Clustering heliostats into fixed groups on a common pod structure as described in Section 2.1 brings a special challenge to the heliostat field layout optimization [19].

Aiming strategy optimization is a way of optimizing the performance of heliostat fields that is closely related to the receiver performance. All heliostats aiming to one single point on the receiver surface would cause the receiver material to melt. Hence, an aiming strategy is not only used for increasing the plant efficiency but it is indispensable in a solar tower power plant. For an optimal efficiency, the flux distribution on the receiver surface needs consider the receiver geometry and operational state. This will be discussed in Section 7.2. Aiming strategies are handled by several works including [4, 25].

A very new approach of optimizing the costs of the heliostat field is the optimization of the cable routing between the heliostats. Here, different cable types are considered, namely data and power cables. An optimized routing can reduce the cabling cost significantly [43].

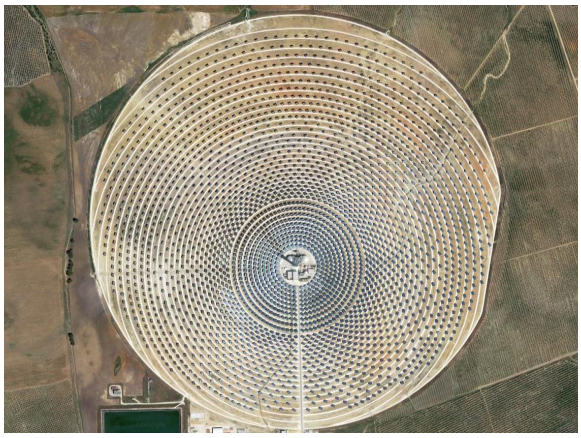

(a) Gemasolar, Spain

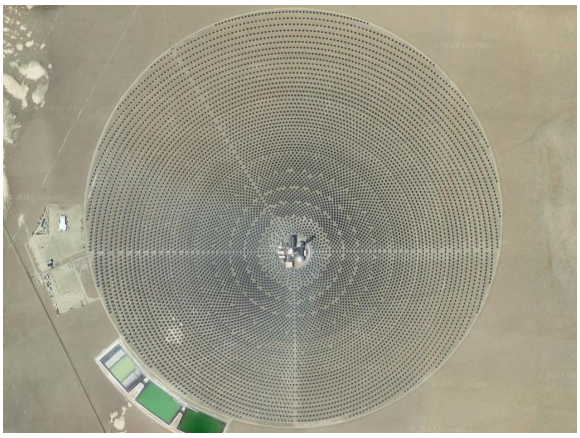

(b) Crescent Dunes, USA

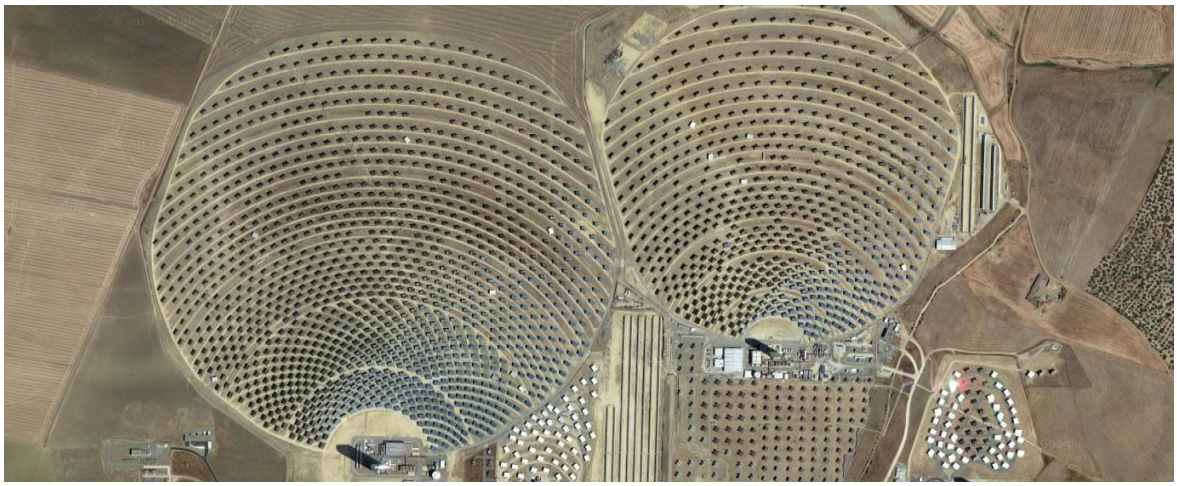

(c) PS20 and PS10, Spain

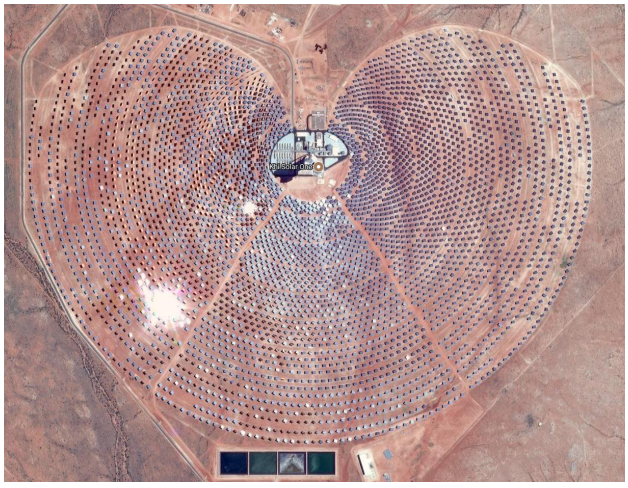

(d) Khi Solar One, South Africa

(e) Jülich Solar Tower, Germany

Figure 11: Satellite Photos of Heliostat Field Layouts [29].

3 Thermal Receiver

The receiver on top of the solar tower is the device that collects the concentrated solar radiation of the heliostat field. It is the first component in a solar tower power plant that converts energy from one form into another, namely radiant energy into thermal energy, i.e., inner energy of a heat transfer medium. There are very different approaches of receiver designs. Furthermore, different heat transfer media are used, e.g., ambient air [32], pressurized air [37], water/steam [24], particles [51], or molten salt [35]. In this work, we will only consider receivers that use molten salt as a heat transfer medium, in the following called HTF.

There are mainly three different receiver geometries used in practice. These are the flat (tilted), cylindrical cavity, and cylindrical external receivers (see Figure 12). Flat and cavity receivers are used for northern or southern fields, e.g., PS10 in Southern Spain [44] or the Jülich Solar Tower in Germany [32]. For heliostat fields all around the tower (see Figures 11a and 11b), generally cylindrical external receivers are used, e.g., Gemasolar [9]. This is the type of receiver, we will focus on in this work.

(a) (b) (c)

Figure 12: Different solar receiver geometries: (a) Flat tilted receiver of the Helio100 test facility in South Africa [62]. (b) Cavity Receiver as used in the PS10 power plant in Southern Spain [15]. (c) Cylindrical external receiver of the Crescent Dunes Plant in Nevada, USA [68].

In the following, a thermal model for external cylindrical molten salt receivers will be described in detail. Since the target of the model is the analysis of a solar tower power plant for use in plant optimization, the thermal receiver model shall be kept as simple as possible. The desired output is the overall thermal power output depending on the incident radiation. We will start with a general non-simplified model description, discuss simplifications and according assumptions which then lead to the simplified model.

3.1 Receiver Geometry

As mentioned above, the receiver considered in this work is a cylindrical external receiver with molten salt as a heat transfer medium. We will stay with the geometry description of the Solar One and Solar Two receiver design as provided by Pacheco

et al. [45] and Wagner [66]. The (approximately) cylindrical receiver consists of several rectangular panels of full receiver height. Each panel is made up of multiple vertical parallel tubes, see Figure 13. The HTF flows either upwards or downwards through the tubes of a panel. The flow direction alternates panel-wise. According to Wagner [66], different possible flow patterns are implemented into the model. However, in this work only the flow pattern of the Solar Two receiver will be used [see 66, Figure 20]: There are two separate HTF flows entering the two northernmost receiver panels, passing through the neighboring panels up to the westernmost and easternmost panels, respectively. Then the flows change from west to east, and vice-versa, and continue flowing southwards through their neighboring panels until they reach the southernmost panels where they are expected to have reached the desired output temperature and leave the receiver system.

The number of tubes per panel is not explicitly stated. Instead it can be computed from the known diameters of the full cylinder and the tubes, respectively. The following equation can be used for this:

$$N_{tubes/panel} = \left\rfloor \frac{\pi \cdot D_{rec}}{D_{tube,outer} \cdot N_{panels}} \right\lceil \tag{3.1}$$

where $\lfloor \cdot \rceil$ is the nearest integer function defined as

$$\lfloor x \rceil := \lfloor |x| + 0.5 \rfloor \cdot \operatorname{sgn} x. \tag{3.2}$$

The position of each tube is specified through its azimuth angle φ. The azimuth is defined to be 0 in Southern direction and measured counter-clockwise, i.e., $\varphi = 90°$ is the eastern direction.

3.2 General Thermal Model Description

The mathematical equations for describing the flow through, the flow around, and the temperature distribution inside the receiver are described here, following the description by Garbrecht [26, Chapter 2]. The air flow around the receiver, as well as the flow of the HTF through the receiver tubes, is described by the Navier-Stokes equations (3.3) for mass, momentum and energy

$$\frac{\partial \rho}{\partial t} + \boldsymbol{\nabla} \cdot (\rho \boldsymbol{v}) = 0 \tag{3.3a}$$

$$\frac{\partial (\rho \boldsymbol{v})}{\partial t} + \boldsymbol{\nabla} \cdot (\rho \boldsymbol{v}\boldsymbol{v}) = -\boldsymbol{\nabla} p + \boldsymbol{\nabla} \cdot (\mu \boldsymbol{\tau}) + \rho \boldsymbol{g} \tag{3.3b}$$

$$\frac{\partial (\rho e)}{\partial t} + \boldsymbol{\nabla} \cdot (\rho e \boldsymbol{v}) = -\boldsymbol{\nabla} \cdot (p \boldsymbol{v}) + \boldsymbol{\nabla} \cdot (k \boldsymbol{\nabla} T) \tag{3.3c}$$

valid in the corresponding domains Ω_{air} and Ω_{htf}. We have the stress tensor

$$\boldsymbol{\tau} = \left(\boldsymbol{\nabla} \boldsymbol{v} + (\boldsymbol{\nabla} \boldsymbol{v})^{\mathsf{T}} - \frac{2}{3} \boldsymbol{I} (\boldsymbol{\nabla} \cdot \boldsymbol{v}) \right) \tag{3.4}$$

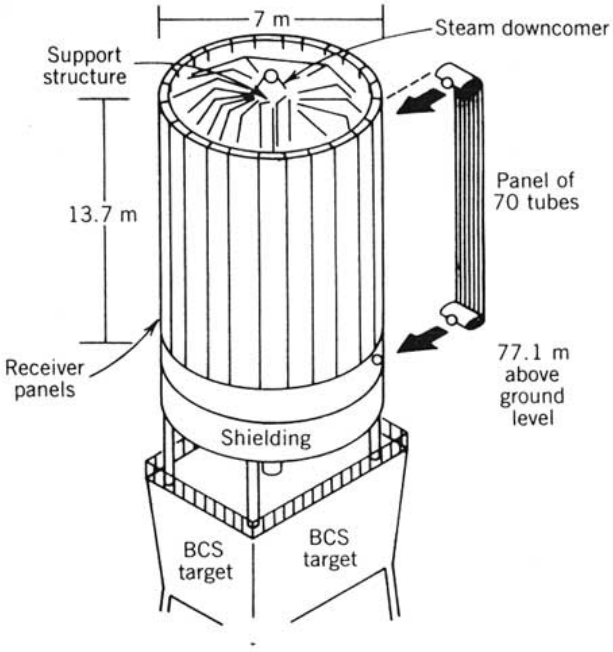

Figure 13: Schematic view of the Solar One receiver [63].

where $\boldsymbol{I}$ denotes the identity matrix, and the gravity vector

$$\boldsymbol{g} = (0 \quad 0 \quad -g)^{\mathsf{T}}. \tag{3.5}$$

The temperature distribution inside the receiver tube walls can be modeled by a conservation equation for the enthalpy:

$$\frac{\partial \rho h}{\partial t} = \boldsymbol{\nabla} \cdot (k \boldsymbol{\nabla} T) + S \tag{3.6}$$

valid in Ω_{wall}. Here, S is a representative for sources and sinks that includes the incident radiation and the energy loss due to radiation.

The three separate systems need to be coupled by boundary conditions, such as equality of temperature and heat flux on the boundaries of neighboring domains $\Gamma_{htf,wall}$ and $\Gamma_{wall,air}$ (see Figure 14).

3.3 Assumptions for the Simplified Model

As mentioned in the introduction of this section, we don't want to model the receiver in detail: We are only interested in the thermal energy output based on the incident radiation. The actual flow distributions of the surrounding air and the HTF are not of interest for the techno-economic assessment.

For the simple model that is required we also don't need any time dependencies. Startup and Shutdown processes won't be modeled here as we are considering a steady

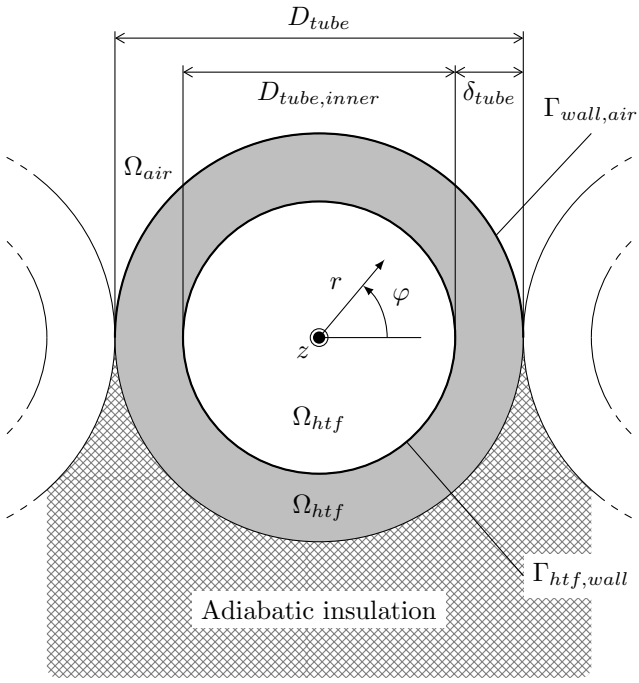

Figure 14: Measurements and coordinate system of a receiver tube (cross sectional view).

state at each point in time. Even for cloud passages, the changes in the received radiation are assumed to be small enough for the steady state assumption to be valid.

Since we are assuming steady state, the tubes already have reached their temperature so that the full power going into the receiver system is absorbed by the HTF. For the same reason the heat conduction inside the tubes as well as between neighboring tubes is neglected.

The receiver will be discretized in so-called pieces for the actual computation (see Section 3.5). In each of those pieces, the characteristic quantities (e.g., the surface temperature) are averaged.

3.4 Simplified Receiver Model

The simplified receiver model, as proposed by Wagner [66] in 2008 and still used in the System Advisor Model (SAM) [41], assumes the HTF to absorb the whole power of the receiver system, see above. With this assumption, the energy balance (3.7) applies.

$$\dot{Q}_{htf} = \dot{Q}_{inc} - \left(\dot{Q}_{ref} + \dot{Q}_{rad} + \dot{Q}_{conv}\right) \tag{3.7}$$

In the following, we will call heat flows of the whole system $\dot{Q}$ and the heat flows of any subsystem, i.e., a piece of the receiver, $\dot{q}$. This results in $\dot{Q}$ being the sum of all $\dot{q}_i$. Length-related quantities will be marked with a prime, area-related quantities with a double prime (e.g., $\dot{q}''_{inc}$ [Wm^{-2}] is the area-related incident radiation, also called flux).

Models for the incident radiation and heat losses are presented in Sections 3.4.1 to 3.4.4. The models are valid for an arbitrary piece of the receiver with area A. The method of discretizing the receiver surface is described in Section 3.5.

3.4.1 Incident Radiation

The incident radiation of the receiver is obtained by the flux map that previously needs to be computed by a ray tracer. Ambient radiation is not considered here as it is much smaller than the concentrated direct radiation from the heliostat field. However, it will be considered in the computation of radiation losses ($\rightarrow$ 3.4.3).

The receiver flux map is defined as

$$\dot{q}''_{inc} = \dot{q}''_{inc}(x, \varphi). \tag{3.8}$$

The flux of a receiver piece (one cell in a receiver discretization) is then obtained by integrating the flux map over the corresponding area:

$$\dot{q}_{inc} = \int_{\delta\varphi} \int_{\delta x} \dot{q}''_{inc}(x, \varphi) \mathrm{d}x \mathrm{d}\varphi. \tag{3.9}$$

3.4.2 Reflection

The receiver cannot absorb the full incident power. There are fractions for absorptivity α, reflectivity ρ and transmissivity τ that sum up to 1 [34]. Since the solar tower receiver is opaque, the transmissivity τ is 0, so $\rho = 1 - \alpha$. In the following, we will drop the symbols ρ and τ and express the reflectivity in terms of α.

Heat loss due to reflection at each position of the receiver surface is simply described by

$$\dot{q}_{ref} = (1 - \alpha) \cdot \dot{q}_{inc}. \tag{3.10}$$

The local energy balance can be simplified from

$$\dot{q}_{htf} = \dot{q}_{inc} - (\dot{q}_{ref} + \dot{q}_{rad} + \dot{q}_{conv}) \tag{3.11a}$$

to

$$\dot{q}_{htf} = \alpha\, \dot{q}_{inc} - (\dot{q}_{rad} + \dot{q}_{conv}). \tag{3.11b}$$

When using a non-gray, or selective, surface material, the absorptivity is wavelength dependent, and should be considered in the notation. Here, λ_{sun} is used representative for the solar spectrum on the surface of the earth.

$$\dot{q}_{ref} = (1 - \alpha(\lambda_{sun})) \cdot \dot{q}_{inc}. \tag{3.12}$$

3.4.3 Radiation

The hot receiver surface emits radiation to the environment which depends on the temperature of the surface and its emissivity ε. For the emissivity, Kirchhoff's law (3.13) applies: This means that for each wavelength of light, the emissivity corresponds to the absorptivity [34].

$$\varepsilon(\lambda) = \alpha(\lambda) \tag{3.13}$$

Since the temperature of the environment is not zero, this needs to be considered. It is assumed that the environment is equally divided by the horizon. Below the horizon, the environment has the ambient temperature T_{amb}, while for the upper half, i.e., the sky, the temperature is determined using Equation (3.14) given by Duffie and Beckman [20]. [66]

$$T_{sky} = T_{amb} \Bigg(0.711 + 0.0056\,(T_{dp} - 273.15) + 0.000073\,(T_{dp} - 273.15)^2 + 0.013 \cos\left(\pi \left(\frac{180 - h \cdot 15}{180}\right)\right)\Bigg)^{1/4} \tag{3.14}$$

Here, the temperatures T_{sky}, T_{amb}, and T_{dp} are given in Kelvin. T_{dp} is the ambient dew point temperature, h denotes the solar time in hours which is 0 at solar noon, negative in the morning, and positive in the afternoon.

The radiation towards the sky is computed as

$$\dot{q}_{rad,sky} = \frac{1}{2}\,\sigma\,\varepsilon\,A\left(T_w^4 - T_{sky}^4\right), \tag{3.15}$$

where $\frac{1}{2}$ is the view factor, i.e., half the radiation from the receiver surface is in the direction of the sky, see above. σ denotes the Stefan-Boltzmann constant with $\sigma = 5.67 \cdot 10^{-8}\,\mathrm{Wm^{-2}\,K^{-4}}$. This can also be expressed in terms of a heat transfer coefficient:

$$\begin{aligned} \dot{q}_{rad,sky} &= \frac{1}{2}\,h_{rad,sky}\,A\,(T_w - T_{sky}) \\ \text{with} \quad h_{rad,sky} &= \sigma\,\varepsilon\left(T_w^2 + T_{sky}^2\right)(T_w + T_{sky}) \end{aligned} \tag{3.16}$$

The same equations apply for the radiation towards the ground:

$$\begin{aligned} \dot{q}_{rad,amb} &= \frac{1}{2}\,\sigma\,\varepsilon\,A\left(T_w^4 - T_{amb}^4\right) \\ &= \frac{1}{2}\,h_{rad,amb}\,A\,(T_w - T_{amb}) \\ \text{with} \quad h_{rad,amb} &= \sigma\,\varepsilon\left(T_w^2 + T_{amb}^2\right)(T_w + T_{amb}) \end{aligned} \tag{3.17}$$

The full radiation loss is then simply the sum of both [66], i.e.,

$$\dot{q}_{rad} = \dot{q}_{rad,sky} + \dot{q}_{rad,amb}. \tag{3.18}$$

For minimizing heat loss due to radiation, it is advantageous to use selective materials, as mentioned previously, so that absorptivity (and emissivity at the same time) is large in the wave length range of the sun's radiation while emissivity is low in the range of wavelengths that are emitted at typical receiver surface temperatures.

3.4.4 Convection

Convection is the dissipation of heat through moving fluids (in our case air). It can be divided into natural and forced convection. Forced convection is due to a flowing fluid while natural convection depends on gravity and thermal buoyancy, or uplift.

Convection in general can be computed similar to Fourier's law of heat conduction as a product of heat transfer coefficient, surface area and temperature difference:

$$\dot{Q}_{conv} = h_{conv}\, A\, (T_w - T_{film}). \tag{3.19}$$

The film temperature used here is the average temperature of receiver surface and free stream, see Equation (3.20).

In the following, the separate computation of forced and natural convection coefficients is discussed, followed by the combination of both into a mixed convection coefficient.

$$T_{film} = \frac{T_w + T_{amb}}{2} \tag{3.20}$$

Forced Convection The forced convection coefficient $h_{conv,for}$ depends heavily on the wind velocity v_{wind} and thus also on the value of the Reynolds number $\mathrm{Re}_{conv,for}$ given by Equation (3.21) [58], see Figure 15. Here, ρ_{film} and μ_{film} are the density and the dynamic viscosity of air at film temperature T_{film}, respectively,

$$\mathrm{Re}_{conv,for} = \rho_{film} v_{wind} \frac{D_{rec}}{\mu_{film}}. \tag{3.21}$$

The Reynolds number can now be used to compute the Nusselt number which corresponds to the amplification of the heat loss due to convection compared to basic heat conduction. For this, we use equation (3.23) developed by Siebers and Kraabel [58]. The symbol k_s is the roughness of the receiver surface. Siebers and Kraabel [58] recommend using the receiver tube radius as a value for k_s so that we have

$$\frac{k_s}{D_{rec}} = \frac{D_{tube}}{2D_{rec}}. \tag{3.22}$$

$\underline{k_s/D_{rec} = 0 \text{ (a smooth cylinder)}}$

$$\text{(all Re)} \qquad \mathrm{Nu} = 0.3 + 0.488 \cdot \mathrm{Re}^{0.5} \left(1 + \left(\frac{\mathrm{Re}}{282000}\right)^{0.625}\right)^{0.8} \tag{3.23a}$$

$\underline{k_s/D_{rec} = 75 \cdot 10^{-5}}$

$$\begin{aligned} &(\mathrm{Re} \leq 7 \cdot 10^5) && \text{use smooth cylinder correlation (3.23a)} \\ &(7 \cdot 10^5 < \mathrm{Re} < 2.2 \cdot 10^7) && \mathrm{Nu} = 2.57 \cdot 10^{-3} \cdot \mathrm{Re}^{0.98} \end{aligned} \tag{3.23b}$$

$$(\mathrm{Re} \geq 2.2 \cdot 10^7) \qquad \mathrm{Nu} = 0.0455 \cdot \mathrm{Re}^{0.81} \tag{3.23c}$$

$\underline{k_s/D_{rec} = 300 \cdot 10^{-5}}$

$$(\mathrm{Re} \leq 1.8 \cdot 10^5) \qquad \text{use smooth cylinder correlation (3.23a)}$$
$$(1.8 \cdot 10^5 < \mathrm{Re} < 4 \cdot 10^6) \qquad \mathrm{Nu} = 0.0135 \cdot \mathrm{Re}^{0.89} \tag{3.23d}$$
$$(\mathrm{Re} \geq 4 \cdot 10^6) \qquad \mathrm{Nu} = 0.0455 \cdot \mathrm{Re}^{0.81} \tag{3.23c}$$

$\underline{k_s/D_{rec} = 900 \cdot 10^{-5}}$

$$(\mathrm{Re} \leq 1.0 \cdot 10^5) \qquad \text{use smooth cylinder correlation (3.23a)}$$
$$(\mathrm{Re} > 1.0 \cdot 10^5) \qquad \mathrm{Nu} = 0.0455 \cdot \mathrm{Re}^{0.81} \tag{3.23c}$$

The heat transfer coefficient for forced convection is then

$$h_{conv,for} = \mathrm{Nu}_{conv,for} \frac{k_{film}}{D_{rec}} \tag{3.24}$$

with k_{film} the conductivity of air at film temperature T_{film}.

Although the correlation developed by Siebers and Kraabel is more than 30 years old at the date of the publication of this work, there is still no other simple correlation for forced or even mixed convection. There are several projects computing the convection losses of solar receivers [see e.g., 12, 26, 65, 73]. However, almost none of them considers surface roughness. The study of Garbrecht [26] considers surface roughness in a mixed convection computational fluid dynamics (CFD) simulation, but since the problem is very complex, the geometry was simplified to a flat plate in parallel flow situation which still resulted in a huge computational effort. Uhlig et al. [65] showed that the relative error of the receiver efficiency computed with the correlation of Siebers and Kraabel [58] doesn't exceed 0.5 %.

Figure 15 shows the Nusselt number for forced convection $\mathrm{Nu}_{conv,for}$ as a function of the Reynolds number $\mathrm{Re}_{conv,for}$. The correlation by Siebers and Kraabel is compared to those by Hilpert [33], Churchill and Bernstein [13], and Whitaker [71]. It can be seen that the Nusselt number, and therewith the convective heat loss, is much higher using the correlation (3.23) which is the only correlation considering surface roughness, than using the other correlations from literature. For generating Figure 15, the following parameters were used: $T_{wall} = 837\,\mathrm{K}$, $T_{amb} = 293\,\mathrm{K}$, $p_{amb} = 1 \cdot 10^5\,\mathrm{Pa}$, $D_{rec} = 8.15\,\mathrm{m}$, $D_{tube} = 25\,\mathrm{mm}$.

The correlation of Hilpert is only defined for small values of $\mathrm{Re}_{conv,for}$. The discontinuities in the Siebers and Kraabel model come from the case distinction in Equation (3.23).

Natural Convection The cylindrical receiver can be assumed as a flat plate for the computation of a natural convection coefficient [58]. After Kneer [34], this assumption is valid if the receiver diameter is much greater than the maximal thickness of the boundary layer developed by natural convection. The rule of thumb $\frac{D_{rec}}{h_{rec}} > 35 \cdot \mathrm{Gr}_{conv,nat}^{-1/4}$

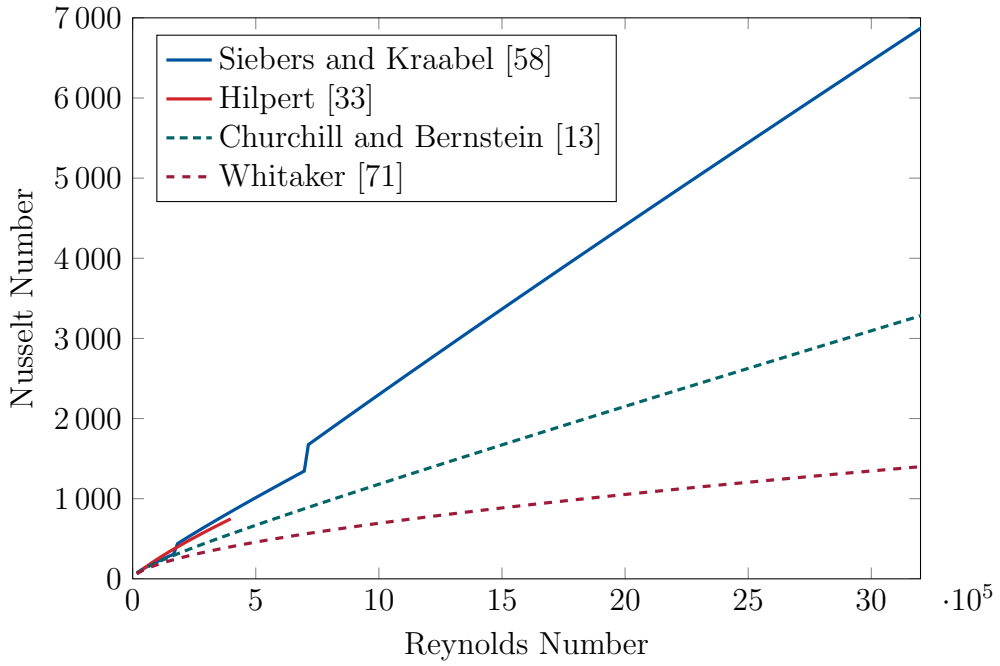

Figure 15: Nusselt number for forced convection at different Reynolds numbers [cf. 66].

is given with the Grashof number $\mathrm{Gr}_{conv,nat}$ from Equation (3.25) [58]. This inequality is fulfilled for receivers similar to the Solar Two receiver. With the Grashof number, the Nusselt number for natural convection can be computed using correlation (3.26), which was developed by Siebers et al. [59] by fitting experimental data. Equation (3.27) for the natural convection coefficient corresponds to Equation (3.24).

$$\mathrm{Gr}_{conv,nat} = g\beta_{amb}\left(T_w - T_{amb}\right)\frac{h_{rec}^3}{\nu_{amb}^2} \tag{3.25}$$

$$\mathrm{Nu}_{conv,nat} = 0.098 \cdot \mathrm{Gr}_{conv,nat}^{1/3}\left(\frac{T_w}{T_{amb}}\right)^{-0.14} \tag{3.26}$$

$$h_{conv,nat} = \mathrm{Nu}_{conv,nat}\frac{k_{film}}{h_{rec}} \tag{3.27}$$

Mixed Convection Mixed convection is a topic of current research as it is not fully understood yet and very costly to simulate, especially when considering turbulence and surface roughness [26]. In this work, we will consider the same simplified relation as Wagner [66] for getting a mixed convection coefficient from the previously obtained coefficients for only-forced and only-natural convection. The correlation (3.28) is taken from Siebers and Kraabel [58] who also recommend using $a = 3.2$ for the exponent.

$$h_{conv,mixed} = \left(h_{conv,for}^a + h_{conv,nat}^a\right)^{1/a}. \tag{3.28}$$

Wall Temperature The wall surface temperature T_w that is used for the loss calculations above is computed from the heat conductivity of the tube material and the convection effects of the HTF flow inside the tube. This is expressed by two different thermal resistances R_{wall} and $R_{conv,inner}$. The thermal resistance over the tube wall R_{wall} describes the restriction of heat flow through the receiver tube wall due to the conductivity. It is defined as [34]

$$R_{wall} = \frac{\ln\left(\frac{D_{tube}}{D_{tube,inner}}\right)}{2\,\pi\,k_{wall}\,\Delta z} \tag{3.29}$$

with the conductivity k_{wall} evaluated at the average wall temperature (not T_w!).

The convective thermal resistance is given by Equation (3.30) [66] with the convection coefficient $h_{conf,inner}$ as computed before, see Equation (3.31). The Nusselt number for turbulent flows through pipes is then given by Equation (3.32) [28]. ξ is the drag coefficient. It is defined in Petukhov [47] and Gnielinski [28] depending on the relative roughness of the inner tube wall $\frac{\varepsilon}{D_{tube,inner}}$ with the absolute roughness explicitly stated in Equation (3.34), see also [41].

$$R_{conv,inner} = \frac{2}{\pi\,h_{conv,inner}\,D_{tube,inner}\,\Delta z} \tag{3.30}$$

$$h_{conv,inner} = \mathrm{Nu}_{conv,inner}\,\frac{k_{htf}}{D_{tube,inner}} \tag{3.31}$$

$$\mathrm{Nu}_{conv,inner} = \frac{(\xi/8)\,(\mathrm{Re}_{inner} - 1000)\,\mathrm{Pr}_{inner}}{1 + 12.7\,\sqrt{\xi/8}\left(\mathrm{Pr}_{inner}^{2/3} - 1\right)}\left(1 + \left(\frac{D_{tube,inner}}{h_{rec}}\right)^{0.7}\right) \tag{3.32}$$

$$\mathrm{Pr}_{conv,inner} = \frac{\eta_{htf}\,c_{p,htf}}{k_{htf}} \tag{3.33}$$

$$\frac{\varepsilon}{D_{tube,inner}} = \frac{1.5\cdot 10^{-3}\,\mathrm{mm}}{D_{tube,inner}} \tag{3.34}$$

With R_{wall} and $R_{conv,inner}$ given, the wall surface temperature can be computed using the following equation [34, 66]:

$$T_w = T_{htf} + \underbrace{\dot{m}_{htf}\cdot c_{p,htf}\cdot \Delta T_{htf}}_{=\dot{q}_{htf}}\cdot(R_{wall} + R_{conv,inner}). \tag{3.35}$$

3.5 Implementation

The thermal receiver model was implemented in C++ during the course of this work. In the equations of the above model description, it is kept open on what surfaces the losses are computed. This shall be handled here.

3.5.1 Discretization

As the receiver is made up of panels of full receiver height, the receiver can already be seen as discretized in circumferential direction by design. In vertical direction, the

receiver is discretized equidistantly into pieces that will also be called discretization cells later on. Each cell has different state variables such as in- and outflow temperatures, average temperature, surface temperature, and a local film temperature. The thermal losses are then computed for each cell individually and the local energy balance (3.11) is solved for each cell.

However, for the convection losses, massively simplified models are used, and the cylindrical receiver must be considered as a whole in these models, convection coefficients aren't computed piece-wise. For forced convection, the whole receiver is averaged in order to find the overall forced convection loss. Natural convection happens in vertical direction and depends on the size of the considered area, so also here, the losses can't be computed for each cell individually. The surface temperatures are, thus, averaged for each panel of the receiver.

The receiver pieces are coupled according to the flow pattern. This means that the inflow temperature of each piece corresponds to the outflow temperature of the previous receiver piece. The first piece is, obviously, entered by cold salt while the outflow of the last piece has the desired receiver output temperature.

3.5.2 Iteration

The receiver model as it is described above, is an implicit problem: The losses depend on the surface temperature which again depends on the absorbed power depending on the losses. Hence, the model equations can hardly be solved analytically. An iteration updates the different model quantities until the computed hot salt temperature corresponds to the desired reference hot salt temperature. If the iteration doesn't converge, there is a maximal number of iterations.

4 Thermal Storage

Modern solar tower power plants usually have a thermal storage system, or thermal energy storage (TES). The hot molten salt that is used as a HTF in the receiver system can perfectly be stored, so electricity can be generated whenever it is required, not only during day time. The TES is, therefore, the significant advantage of solar thermal energy systems compared to photovoltaics (PV). It makes solar thermal energy plants capable for the base load and, at the same time, allows covering peaks in the electricity demand.

According to the different approaches of receiver designs and the use of different heat transfer media, there are also different TES concepts. For example, for air receivers, the heat might be stored in a rock bed storage as described by Allen et al. [2]. For the use with particle receiver, the hot particles can be stored directly without the need of another heat exchanger [51] as it is required for air receivers. In general, the storage medium needs to have a high heat capacity which is the case for particles as well as for molten salt.

In this work, there is no actual model of the storage system. Instead, it is assumed that there is enough storage capacity such that electricity can be generated at the times with the highest electricity need, i.e., at the times with the highest reimbursement (tariff of electricity (ToE)).

Figure 16 shows a photo of an installed thermal storage system at the Valle 1/Valle 2 parabolic trough plant in Southern Spain.

Figure 16: Photo of a thermal energy storage system [57].

5 Power Block

The power block, also called power conversion unit (PCU), comprises the components of a conventional thermal power plant. The model contains steam generator, turbine, generator, and the cooling system. Since all these components work together as a whole, we model the power block using a simple lookup table:

From knowing the load and the ambient temperature, the efficiency of the power block η_{pcu} can be looked up and interpolated from the given values. The ambient temperature is, depending on the cooling system, either the dry-bulb temperature or the wet-bulb temperature. Figure 17 shows the dependency of the power block efficiency on the ambient temperature and the load of a 100 $\mathrm{MW_{th}}$ dry-cooling system. The data was provided by TSK Flagsol.

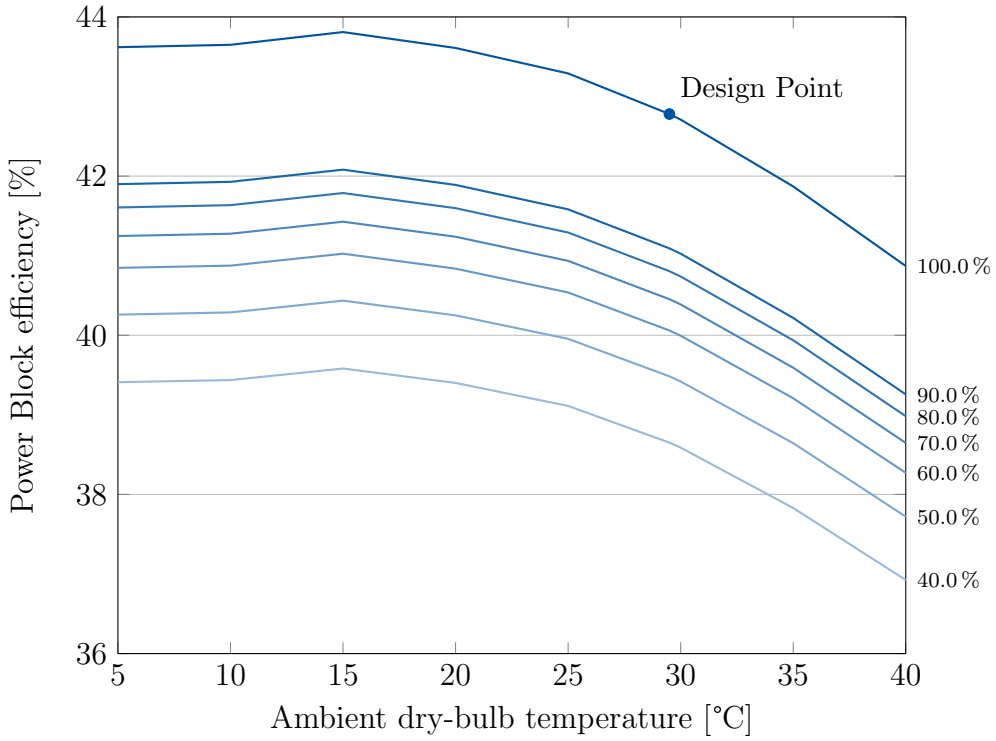

Figure 17: Characteristic Diagram of a 100 $\mathrm{MW_{th}}$ power conversion unit. The lines represent the temperature-dependent efficiencies for different loads.

For the determination of the efficiency at any point, i.e., load-temperature pair, we use bilinear interpolation:

$$\begin{aligned}\eta_{pcu}(l,T) = &\frac{1}{(l_2-l_1)(T_2-T_1)} \\ &\Big(\eta_{pcu}(l_1,T_1)\cdot(l_2-l)(T_2-T) + \eta_{pcu}(l_2,T_1)\cdot(l-l_1)(T_2-T) \\ &\quad + \eta_{pcu}(l_1,T_2)\cdot(l_2-l)(T-T_1) + \eta_{pcu}(l_2,T_2)\cdot(l-l_1)(T-T_1)\Big) \end{aligned} \tag{5.1}$$

where l_1 and T_1 are the next lower values from l and T, respectively, available in the table. l_2 and T_2 are analogously defined as the next higher values.

Figure 18 shows the bilinearly interpolated efficiencies for the values plotted in Figure 17.

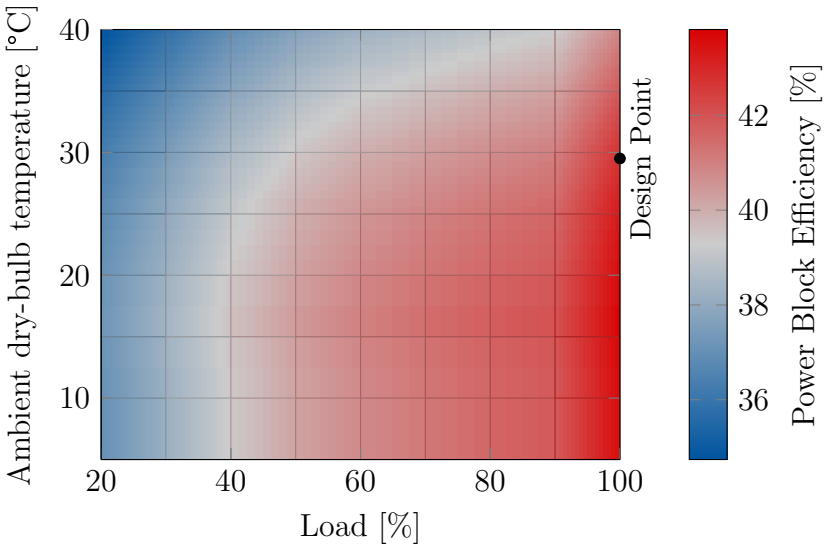

Figure 18: Efficiency of a 100 $\mathrm{MW_{th}}$ power block depending on ambient dry-bulb temperature and load.

6 Economic Model

The costs of a solar tower plant are split into the investment costs, the so-called capital expenditure (CAPEX), and the running costs, so-called operational expenditure (OPEX), that need to be paid for each year or each kWh_{el}. The computation of both CAPEX and OPEX is described in the following.

6.1 Investment Costs

Investment costs are those costs that are paid once. The total investment costs can be summarized in the term capital expenditure (CAPEX).

$$CAPEX = I_{land} + I_{hel} + I_{tower} + I_{rec} + I_{stor} + I_{pcu} \tag{6.1}$$

The CAPEX is expressed in terms of [M$]. According to Augsburger [5] we will call investment costs I and specific costs c.

Sections 6.1.1 to 6.1.2 present concepts that will be used in the calculation of investment costs. The investment costs mentioned in Equation (6.1) are described in Sections 6.1.3 to 6.1.8.

6.1.1 Scaling Effects

When estimating the cost of a new project, experience from previous projects can be employed. From existing projects of different scales, a scale factor s can be obtained that can then be used to scale the costs of a reference project to the scale of the considered project. Equation (6.2) from [53, Appendix B] holds.

$$c_{new} = c_{ref} \cdot \left(\frac{A_{new}}{A_{ref}} \right)^{s} \tag{6.2}$$

with c_{new}, c_{ref} costs of the new project and the reference project, respectively, and A the sizes of both projects. The scaling effect is visualized for different scale factors s in Figure 19.

6.1.2 Volume Effect

Usually, production becomes cheaper with increasing quantities and increasing production experience. This effect is called volume effect and can be modeled by the following equation [53, Appendix B]:

$$c_{new} = c_{ref} \cdot pr^{\log_2 \frac{V_{new}}{V_{ref}}} \tag{6.3}$$

where pr is the so-called progress ratio, an estimate of the cost improvement when doubling the production volume, c_{new} and c_{ref} denote the cost of the considered project and the reference project, respectively, and V are the production volumes. For a short deviation, we start with the definition of the progress ratio

$$pr = \left(\frac{c_{new}}{c_{ref}} \right)^{\frac{1}{n_d}} \tag{6.4}$$

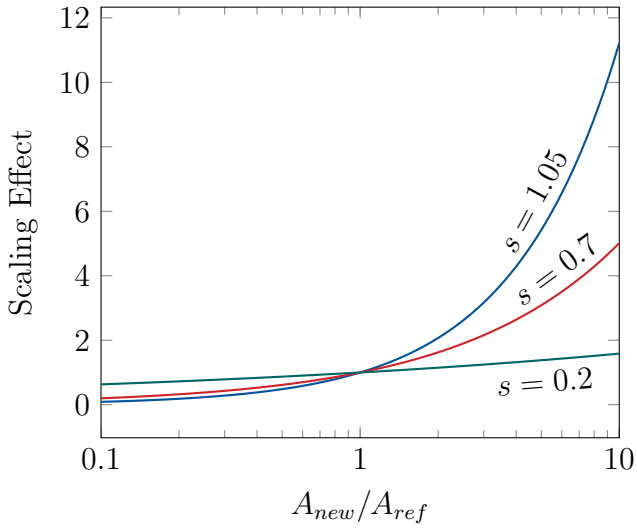

Figure 19: Visualization of the scaling effect for different scale factors.

with the number of doublings n_d that can be expressed in terms of the production volumes V_{ref} and V_{new}:

$$n_d = \log_2 \frac{V_{new}}{V_{ref}}. \tag{6.5}$$

With plugging Equation (6.5) into Equation (6.4) and solving for c_{new} we obtain Equation (6.3). The volume effect can be used in combination with the scaling effect. A visualization of the volume effect for different values of pr can be found in Figure 20.

Now, the basics are defined and we can look at the different components in detail.

6.1.3 Land

The investment costs for the land are divided into costs for the terrain itself and the improvement of the terrain

$$I_{land} = I_{terrain} + I_{improv} \tag{6.6}$$

where $I_{terrain}$ is computed from the cost per square meter and the area of the site

$$I_{terrain} = c_{terrain}\, A_{terrain} \tag{6.7}$$

$$I_{improv} = I_{improv,ref} \cdot \left(\frac{A_{terrain}}{A_{terrain,ref}} \right)^{s_{improv}} \tag{6.8}$$

Augsburger [5] provides values for the reference case and the scaling factor, see Table 3.

6.1.4 Heliostats

The investment costs for the heliostats are composed of several sub-costs: The direct costs $I_{hel,dir}$ including material and labor costs, the optical costs $I_{hel,optic}$ that

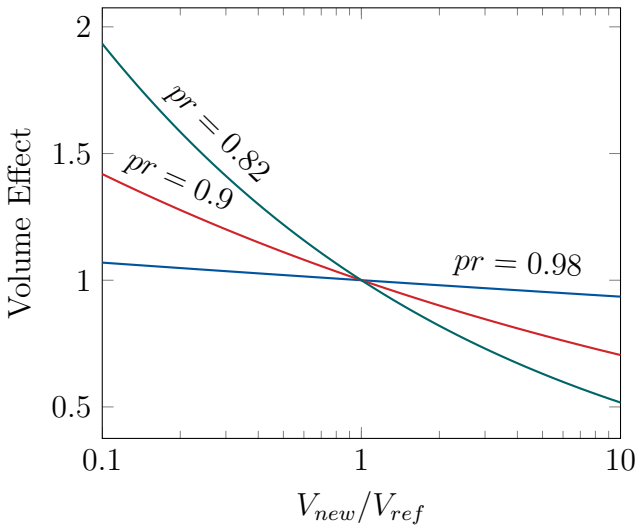

Figure 20: Visualization of the volume effect for different progress ratios.

take account of the heliostats' slope, overhead costs $I_{hel,overhead}$ for management and engineering, and indirect costs $I_{hel,indir}$ for additional tooling.

$$I_{hel} = I_{hel,dir} + I_{hel,optic} + I_{hel,overhead} + I_{hel,indir} \tag{6.9}$$

Direct Costs The direct costs are again split up into sub-costs that are listed in Table 1. For each of these sub-costs $_{hel,dir,i}$ scaling effect, volume effect, and price index are taken into account. The price index pi describes the change in the price from the date of the reference values to the date of the computation.

$$I_{hel,dir} = N_{hel} \cdot c_{hel,dir} \tag{6.10}$$

$$c_{hel,dir} = \sum_i c_{hel,dir,i} \tag{6.11}$$

$$c_{hel,dir,i} = c_{hel,dir,i,ref} \cdot \left(\frac{A_{hel}}{A_{hel,ref}}\right)^{s_{hel,dir,i}} \cdot pr_{hel,dir,i}^{\log_2 \frac{V_{hel}}{V_{hel,ref}}} \cdot pi_{hel,dir,i} \tag{6.12}$$

N_{hel} is the number of heliostats in the field, A_{hel} denotes the heliostat mirror area, and V_{hel} is the production volume of the heliostats which is the number of heliostats N_{hel}. Reference values are provided in Table 1.

Optical Cost The optical cost depends on the average heliostat slope. This is related to the heliostat canting as described in Section 2.1. The reference value $\sigma_{slope,ref}$ is given in Table 3.

$$I_{hel,optic} = N_{hel} \cdot c_{hel,optic} \tag{6.13}$$

$$c_{hel,optic} = 0.01 \cdot 10^{-3} \left(\frac{1}{(\sigma_{slope})^2} - \frac{1}{(\sigma_{slope,ref})^2}\right) A_{hel} \tag{6.14}$$

Table 1: Estimated direct cost parameters of a heliostat [5].

Heliostat direct cost i	$c_{hel,dir,i,ref}$ [\$/u]	$s_{hel,dir,i}$	$pr_{hel,dir,i}$	$pi_{hel,dir,i}$
Foundation	200	0.2274	0.9806	1.0816
Pedestal and structure	3 777	1.4700	0.9900	1.8070
Drives	6 000	0.6000	0.9400	1.3702
Mirrors	4 996	1.0420	0.9700	1.0861
Control and Communications	875	0.2311	0.9600	1.2841
Wiring	877	0.4479	1.0000	1.0302
Shop Fabrication	480	0.4264	0.9800	1.0000
Installation and Checkout	450	0.2610	1.0000	1.0000
Total reference direct costs	17 655			

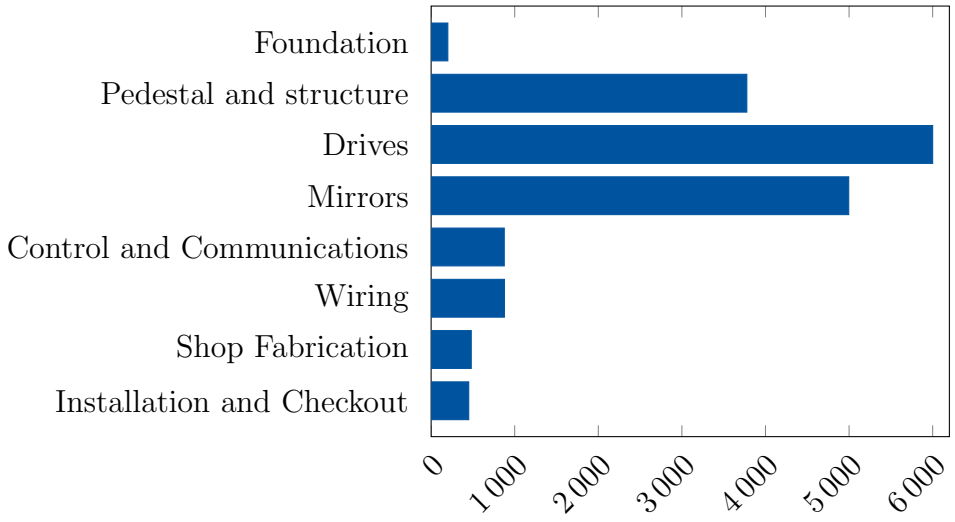

Figure 21: Direct heliostat reference costs.

Overhead The overhead costs of the heliostat contain several costs coming up in the management and engineering of heliostats. It is computed as a share, namely or, of the direct costs $I_{hel,dir}$ with considering a volume effect [5].

$$I_{hel,overhead} = or \cdot I_{hel,dir} \cdot pr_{hel,overhead}^{\log_2 \frac{V_{hel}}{V_{hel,ref}}} \tag{6.15}$$

Indirect Costs Indirect heliostat costs contain costs for the engineering and setup of the heliostats. Similar to the computation of the direct costs, the indirect costs are listed in Table 2 together with the according reference values.

$$I_{hel,indir} = \sum_j I_{hel,indir,j} \tag{6.16}$$

$$I_{hel,indir,j} = I_{hel,indir,j,ref} \cdot \left(\frac{A_{hel}}{A_{hel,ref}} \right)^{s_{hel,indir,j}} \cdot pr_{hel,indir,j}^{\log_2 \frac{V_{hel}}{V_{hel,ref}}} \cdot pi_{hel,indir,j} \quad (6.17)$$

Table 2: Estimated indirect cost parameters of a heliostat [5].

Heliostat indirect cost j	$I_{hel,indir,j,ref}$ [\$]	$s_{hel,indir,j}$	$pr_{hel,indir,j}$	$pi_{hel,indir,j}$
Engineering	250 000	0.9551	0.96	1.2623
Facilities and Tooling	800 000	0.9551	0.86	1.1460
Equipment Lease	200 000	0.9551	0.86	1.1460
Total reference indirect costs	1 250 000			

6.1.5 Tower

The costs for the tower again consider scaling, volume effect and price index. However, there is usually only one tower so the volume effect doesn't play a role.

$$I_{tower} = I_{tower,ref} \cdot \left(\frac{h_{tower}}{h_{tower,ref}} \right)^{s_{tower}} \cdot pr_{tower}^{\log_2 \frac{V_{tower}}{V_{tower,ref}}} \cdot pi_{tower} \quad (6.18)$$

Reference values are provided in Table 3.

6.1.6 Receiver

For the receiver, the same description as for the tower applies: There is typically only one receiver so the volume effect doesn't influence the costs.

$$I_{rec} = I_{rec,ref} \cdot \left(\frac{A_{rec}}{A_{rec,ref}} \right)^{s_{rec}} \cdot pr_{rec}^{\log_2 \frac{V_{rec}}{V_{rec,ref}}} \cdot pi_{rec} \quad (6.19)$$

6.1.7 Storage

Unlike Augsburger [5], the storage system will be considered separately from the PCU. However, the same equation considering scaling effect, volume effect and price index applies.

$$I_{stor} = I_{stor,ref} \cdot \left(\frac{S_{stor}}{S_{stor,ref}} \right)^{s_{stor}} \cdot pr_{stor}^{\log_2 \frac{V_{stor}}{V_{stor,ref}}} \cdot pi_{stor} \quad (6.20)$$

6.1.8 Power Conversion Unit

$$I_{pcu} = \sum_k I_{pcu,k} \quad (6.21)$$

$$I_{pcu,k} = I_{pcu,k,ref} \cdot \left(\frac{S_{pcu,k}}{S_{pcu,k,ref}} \right)^{s_{pcu,k}} \cdot pr_{pcu,k}^{\log_2 \frac{V_{pcu,k}}{V_{pcu,k,ref}}} \cdot pi_{pcu,k} \quad (6.22)$$

Table 3: Reference and scaling values provided by Augsburger [5].

Quantity	Value	Unit	Quantity	Value	Unit
$c_{terrain}$	0.5	[\$/m^2]	$A_{terrain,ref}$	2.8	[km^2]
$I_{improv,ref}$	1.1	[M\$]	s_{improv}	0.3687	[–]
$A_{hel,ref}$	148	[m^2]	$V_{hel,ref}$	1625	[u]
$\sigma_{slope,ref}$	4.14	[mrad]	or	20	[%]
$pr_{overhead}$	0.96	[–]	$I_{tower,ref}$	1.6	[M\$]
$h_{tower,ref}$	75	[m]	s_{tower}	1.797	[–]
pr_{tower}	0.9526	[–]	$V_{tower,ref}$	1	[u]
pi_{tower}	1.0816	[–]	$I_{rec,ref}$	9.1	[M\$]
$A_{rec,ref}$	100	[m^2]	s_{rec}	0.5283	[–]
pr_{rec}	0.9526	[–]	$V_{rec,ref}$	1	[u]
pi_{rec}	1.44	[–]	$I_{stor,ref}$	3.7	[M\$]
$S_{stor,ref}$	88.2	[MWh$_{th}$]	s_{stor}	0.6202	[–]
pr_{stor}	0.9526	[–]	pi_{stor}	2.2	[–]

Table 4: Estimated cost parameters of a power conversion unit [5].

PCU cost k	$S_{pcu,k,ref}$	$I_{pcu,k,ref}$	$s_{pcu,k}$	$pr_{pcu,k}$	$pi_{pcu,k}$
Steam Generator	34.0 MW$_{th}$	1.6 M\$	0.6734	0.9526	1.4400
Steam Turbine and Generator	13.5 MW$_{el}$	8.8 M\$	0.6829	0.9526	1.2971
Cooling System	13.5 MW$_{el}$	7.4 M\$	0.2514	0.9526	1.2254
Master Control	–	1.6 M\$	–	–	1.1690
Total reference PCU costs		19.4 M\$			

6.2 Running Costs: Operations and Maintenance

Augsburger [5] doesn't consider the running costs in detail. He simply assumes a fixed value of 5.4 ¢/(kWh$_{el}$) for the operations and maintenance (O&M) costs. We will, therefore, use the equations of Morin [40] who modeled these costs in detail.

Running costs will be denoted by C. These costs consist of the costs for staff, water, spare parts and insurance, and are summed up to a per-year value, the so-called OPEX with

$$OPEX = C_{staff} + C_{water} + C_{spare} + C_{insur}. \tag{6.23}$$

6.2.1 Staff

The staff is split into staff for the heliostat field and staff for the power block. According to Morin [40], the required heliostat field personnel depends linearly on the area of the site, while the staff for the power block is assumed to be fixed.

$$C_{staff} = (f_{staff,field} \cdot A_{field} + N_{staff,pcu}) \cdot c_{staff} \cdot f_{curr} \tag{6.24}$$

The factor f_{curr} is for converting euros to dollars to stay consistent in one currency. It is required since we are using reference values from different cost models that use different currencies for their reference values. The factor has the unit \$/€ and should be an average of the expected conversion rate during the plant lifetime. Note that the number of required personnel for the heliostat field can be non-integer. This is still considered realistic since part-time jobs are possible. Parameters are provided in Table 5.

6.2.2 Water

The costs for the water depend on the annual energy production (AEP) E_a. From the multiplication with E_a we get an annual cost value.

$$C_{water} = E_a \cdot f_{water} \cdot c_{water} \cdot f_{curr} \tag{6.25}$$

These costs contain the water consumption of the PCU and for mirror cleaning. However, as Morin [40] states, the cost model doesn't consider the total mirror area. This is a reasonable simplification since the water costs are only a very small part of the total annual costs and the mirror cleaning is again only a small percentage of the water consumption (assuming a wet-cooling power block).

For dry-cooling systems, the water consumption is significantly lower. Here, again, parameters are provided in Table 5 and the currency conversion factor f_{curr} as described above is used.

6.2.3 Spare Parts

The cost for spare parts is a fraction of the CAPEX:

$$C_{spare} = CAPEX \cdot f_{spare} \tag{6.26}$$

6.2.4 Insurance

Insurance costs are also dependent on the CAPEX:

$$C_{insur} = CAPEX \cdot f_{insur} \tag{6.27}$$

Table 5: Parameters for the running costs as given by Morin [40].

Quantity	Value	Unit	Quantity	Value	Unit
c_{staff}	48 000	[€/a]	$f_{staff,field}$	$3 \cdot 10^{-5}$	$[\mathrm{m}^{-2}]$
c_{water}	0.5	[€/m^3]	f_{water}	0.295	[m^3/(MWh$_{\mathrm{el}}$)]
f_{spare}	1	[%]	f_{insur}	1	[%]

6.3 Economic Evaluation

In this part, several economic quantities are computed. These depend on the previously described CAPEX and OPEX, the AEP E_a the plant life time N_y, and the interest rate i. In this model, the OPEX is defined as the annual expenditures. To stay consistent with the work of Augsburger [5], we introduce OM as the operational expenditure in [¢/(kWh$_{\text{el}}$)] with

$$OM = \frac{OPEX}{E_a}. \tag{6.28}$$

6.3.1 Levelized Cost of Electricity

The levelized cost of electricity (LCOE), also called leveleized energy cost (LEC), is the most common value for the evaluation of energy costs. It is defined as

$$\begin{aligned} LCOE = \frac{\text{Annual costs}}{\text{Annual energy production}} &= \frac{CAPEX \cdot f_{annuity} + OPEX}{E_a} \\ &= \frac{CAPEX \cdot f_{annuity}}{E_a} + OM \end{aligned} \tag{6.29}$$

with the annuity factor

$$f_{annuity} = \frac{(1+i)^{N_y} \cdot i}{(1+i)^{N_y} - 1}. \tag{6.30}$$

The LCOE is used for an easy comparison of power plants of different types.

6.3.2 Net Present Value

The net present value (NPV) is the sum of all investments, and the present values of all incomes and expenses over the project life time, i.e., the incomes and expenses of each year with considering the interest rate. The NPV is a measure for the total profit, hence, it must be positive. An equation is given by Augsburger [5]:

$$\begin{aligned} NPV &= \frac{(1+i)^{N_y} - 1}{i \cdot (1+i)^{N_y}} (ToE - OM) \cdot E_a - CAPEX \\ &= \frac{ToE - OM}{f_{annuity}} \cdot E_a - CAPEX \end{aligned} \tag{6.31}$$

with the annuity factor $f_{annuity}$ as defined in Equation (6.30).

6.3.3 Internal Rate of Return

The internal rate of return (IRR) is the interest rate with which the sum of incomes and expenses, namely, the NPV, would be zero after the plant life time N_y [5]. For computing the IRR, Equation (6.31) with $NPV = 0$ needs to be solved for i. This can be done using Newton's method where the derivative of NPV with respect to i is needed.

6.3.4 Payback Period

An economic quantity that is interesting for the plant operator is the payback period. It is the amount of time after which the plant starts making profit. In the computation of the payback period the ToE is an important parameter. It is the price that is paid per kWh_{el} on the electricity market. The payback period (in years) is given by the following equation as stated by Augsburger [5]:

$$N_{y,payback} = \frac{\log\left(\frac{(ToE-OM)\cdot E_a}{(ToE-OM)\cdot E_a - CAPEX\cdot i}\right)}{\log\left(1+i\right)} \tag{6.32}$$

7 Validation

In order to check the quality and reliability of the presented models, some tests are performed in the following. However, the validation is not presented for all the models. The power block, for example, only consists of a bilinear interpolation method and was tested. These tests are not worth being described here.

At the end of this section, all models will be brought together into one single annual simulation.

7.1 Heliostat Field

The ray tracer of SunFlower is validated with the softwares SolTrace and Tonatiuh, see e.g., [48, 50]. As this is already described in other publications, this part will be skipped in this work.

7.2 Thermal Receiver

The thermal receiver model is the most complex part of the newly implemented techno-economic simulation model. This is, therefore, also the largest subsection in this part of the work. Since the receiver model is based on the work of Wagner [66], it was also tested against the Fortran code from the digital supplement of Wagner's work. Both codes obtain the same results for one discretization cell per panel.

7.2.1 Panel Discretization

The extended model with more than one discretization cell per panel can't be validated the same way due to the lack of a reference value. Instead, the receiver efficiencies are compared for different numbers of cells and convergence is expected. Figure 22 shows the result of this investigation with using the one-dimensional flux map that is shown in Figure 23b. The two plot lines were created with different termination conditions for the iteration loop. After converging, both lines have a kink after which the iteration doesn't converge so the results aren't reliable anymore. Applying strict termination criteria moves the kink to the left. We use 500 as a maximum number of iterations and a relative error tolerance (for the hot salt temperature) of $1 \cdot 10^{-4}$. In strict mode, these values are set to 200 and $1 \cdot 10^{-12}$, respectively.

Although the plot is converged after a few steps, we can still see a difference in the efficiency compared to using one single cell. In conflict with the result obtained by Wagner [66], it is, therefore, recommended to split the receiver panels into 5 to 10 pieces.

7.2.2 Influence of the Flux Distribution

The distribution of the incoming flux from the heliostat on the receiver surface has a large influence on the receiver operation. This is shown in the following. We are looking at four different flux distributions shown in Figure 23. For the sake of comparability,

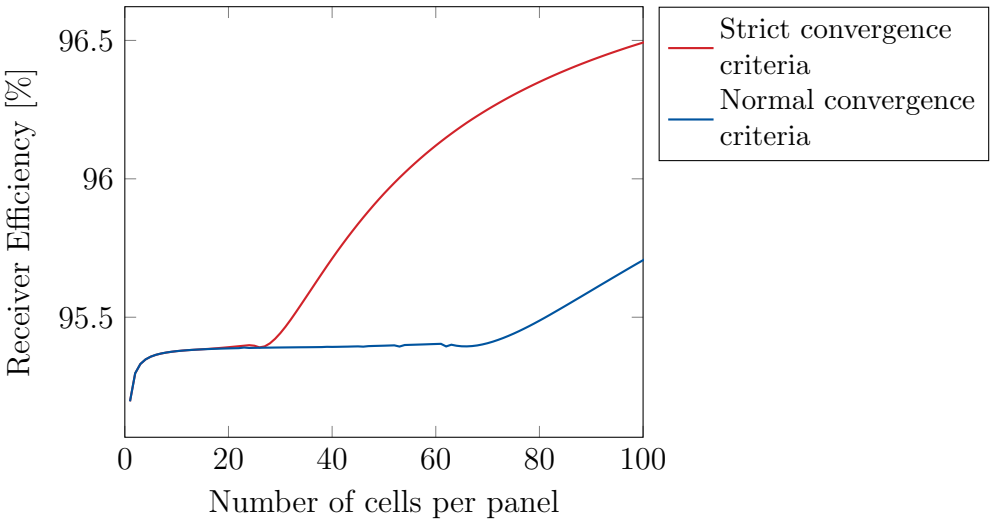

Figure 22: Receiver Efficiency for different numbers of discretization cells using a one-dimensional flux map.

the total incident radiation of all of these distributions is the same. *Uniform Flux* has the same flux at each position on the receiver surface (Figure 23a). The *1D horizontal Flux* map is vertically averaged and changes only in circumferential direction. The highest flux is present on the northern side of the receiver where the HTF flow enters the receiver (Figure 23b). The flux map of test case *1D horizontal Flux inverted* corresponds to *1D horizontal Flux* but now the highest flux is in the south (Figure 23c). The flux map of *1D vertical Flux* only changes vertically with the highest value at half the receiver height. The flux is constant in circumferential direction (Figure 23d).

Table 6 shows the efficiencies for the four test cases. A difference of up to 3 % can be seen between *1D horizontal Flux* and *1D horizontal Flux inverted* which is a lot when looking at power plant efficiencies.

The large difference in the efficiencies comes from the strongly differing temperature distribution that is shown in Figure 24 for all tests. A correlation can be seen between low receiver efficiencies and large areas of high temperatures, compare especially Figure 24b and Figure 24c.

Table 6: Receiver Efficiencies for different flux maps

Test Name	Efficiency
Uniform Flux	94.5531 %
1D horizontal Flux	92.8683 %
1D horizontal Flux inverted	95.7638 %
1D vertical Flux	94.5072 %

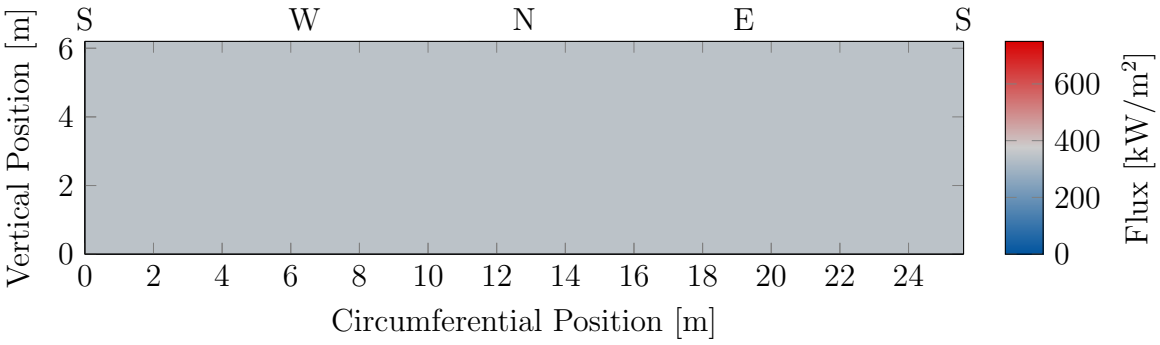

(a) Uniform Flux

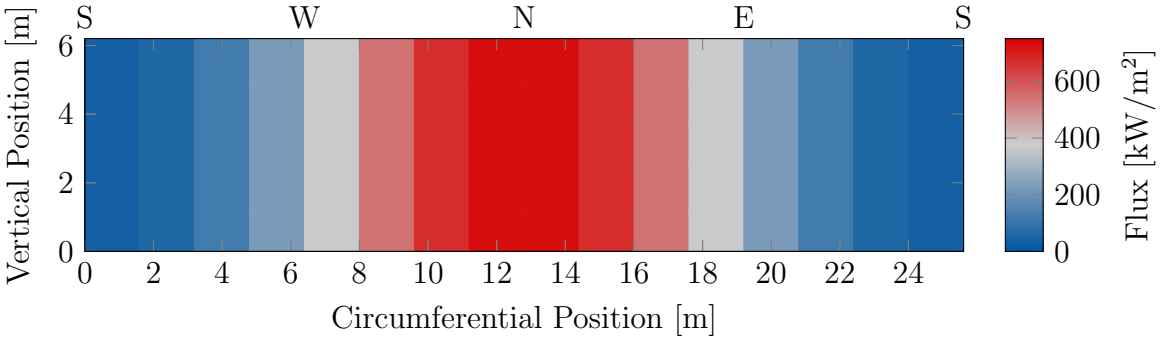

(b) 1D horizontal Flux

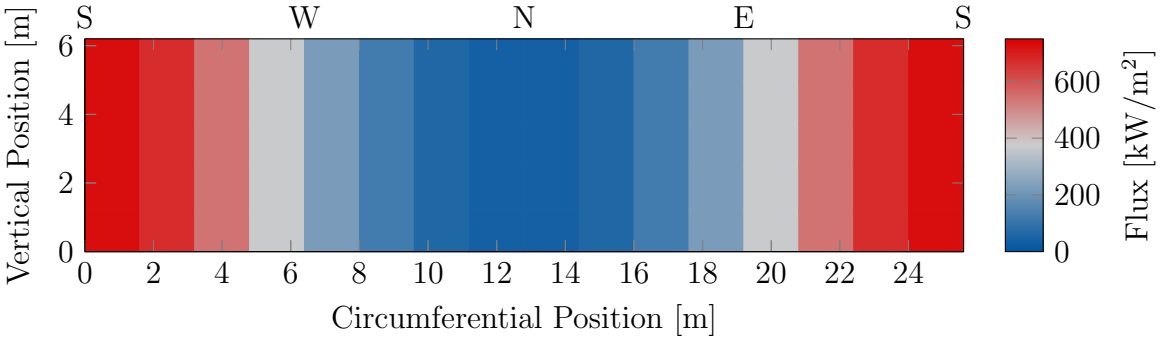

(c) 1D horizontal Flux inverted

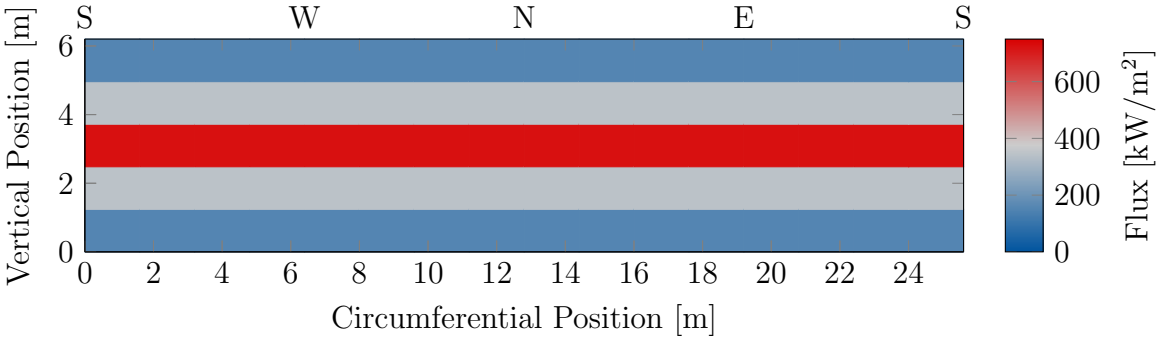

(d) 1D vertical Flux

Figure 23: Flux maps of the receiver test cases.

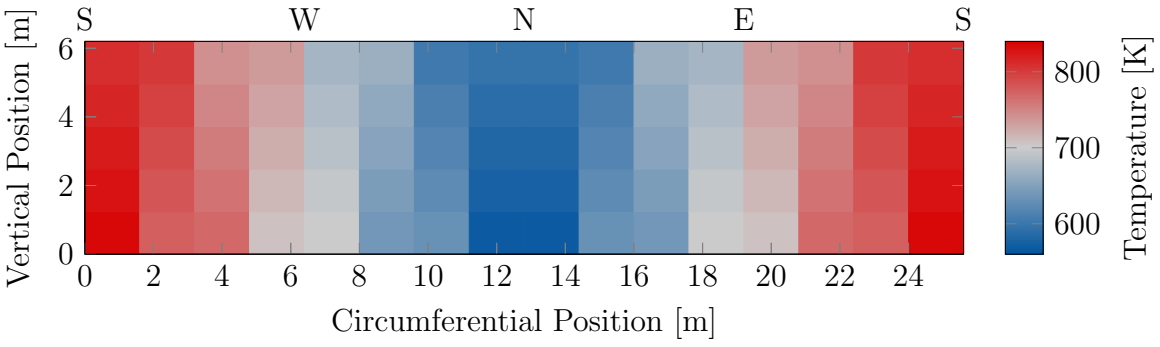

(a) Uniform Flux

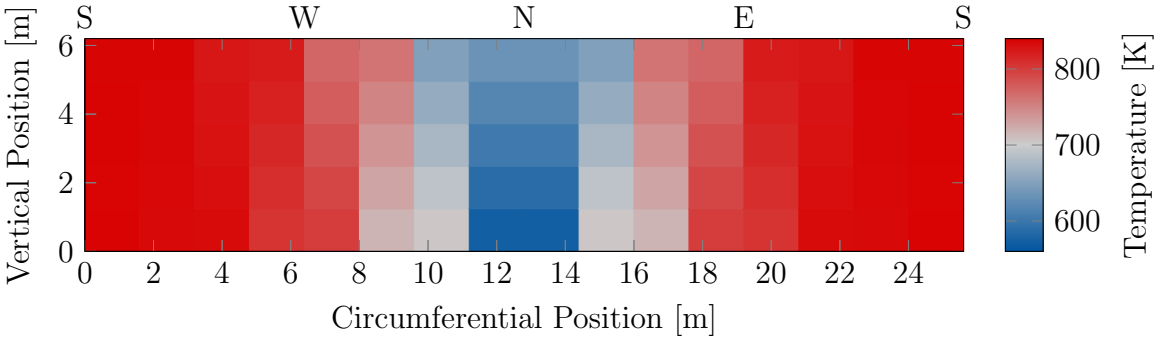

(b) 1D horizontal Flux

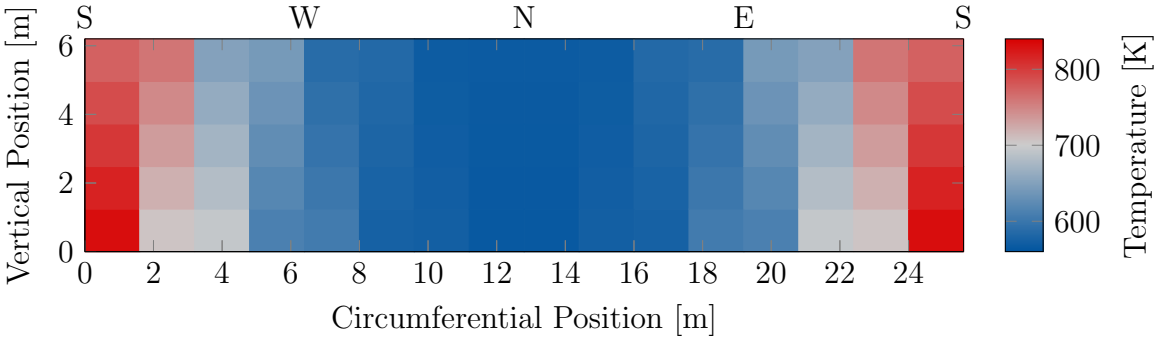

(c) 1D horizontal Flux inverted

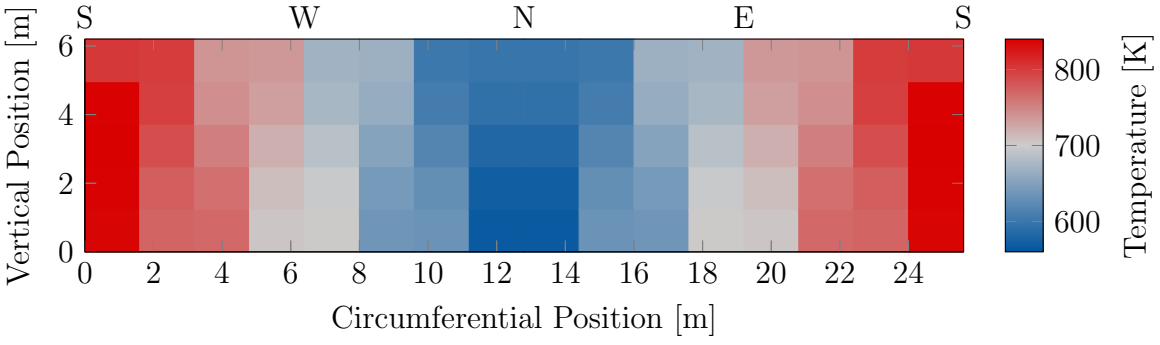

(d) 1D vertical Flux

Figure 24: Temperature distributions for the 4 test cases.

7.3 Economic Model

As an example cost analysis, the investment costs of a plant with 1155 heliostats of 145 m^2. The costs are kept close to those provided by Augsburger [5] as there are no other data available for the author. The result of the cost analysis is shown in Figure 25. The LCOE of the same configuration with an interest rate of 9 % and a

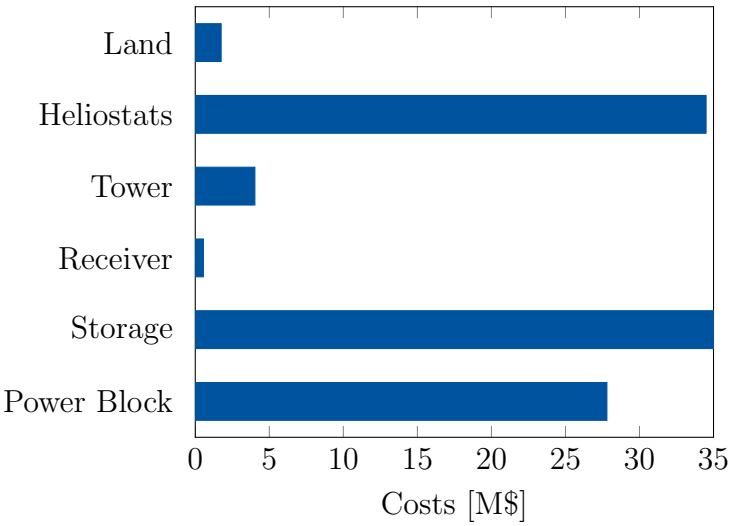

Figure 25: Overview of investment costs for an example plant.

plant lifetime of 25 years is then 23.8778 ¢/(kW h).

7.4 Full Plant Model

An annual simulation was run using the different sub-models as a proof of concept that not only the single models can be evaluated but also a full plant model simulation can be performed. The simulation was based on measured meteorological data from Almería. In Figure 26 the obtained energies of the different sub-models are shown. An example plant with 1155 heliostats of 145 m^2 was used.

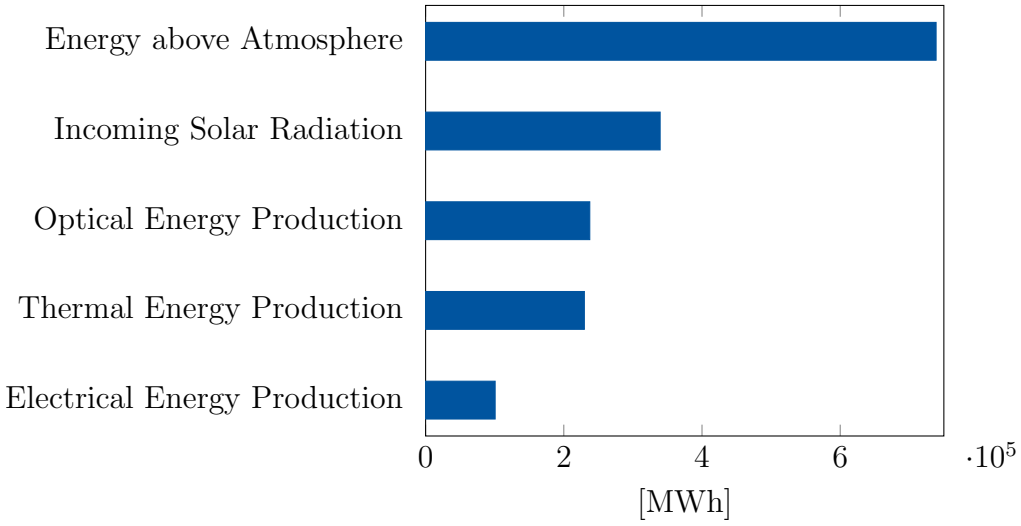

Figure 26: Visualization of the different energies.

8 Conclusion and Outlook

During the course of this work, several performance models for different aspects of a solar tower power plant were implemented. By combining these models, a techno-economic full plant model is obtained. The models are kept efficient enough to use them in heliostat field layout optimization.

For the optical simulation, i.e., the SunFlower ray tracer, triangular heliostat facets were implemented, so that fields of the Stellio heliostat can be evaluated. For this, a two-dimensional Gaussian quadrature rule for triangular domains is used.

The Receiver is modeled on the base of the model implemented in the state-of-the-art software package SAM. This model was the largest part of this work. It was extended by a finer discretization of the receiver panels. Although Wagner [66] proposed using one piece per panel, it was shown in Figure 22 that one should consider multiple pieces per panel.

The TES doesn't have its own model. Instead, it only consists of the assumption that enough energy can be stored such that the annual electricity output is maximized.

The power block is modeled as a whole, i.e., including heat exchanger, steam turbine, electricity generator, and cooling system. For obtaining the power block efficiency for a given ambient temperature and load share, the value is interpolated bilinearly between given table values.

The economic evaluation is a merge of the models of Augsburger [5] and Morin [40]. Investment costs are scaled from reference values from literature with considering manufacturing progress and price trends. The model is capable of returning LCOE, NPV, IRR, and the payback period.

As can be seen in Figure 26, the models work smoothly together as a full plant model in an annual simulation.

The aim of the work was fulfilled by creating a techno-economic model that returns several different output quantities: In addition to the optical energy, thermal energy, electrical energy and economic quantities can be used as objective functions in an optimization. Then, also quantities like the number of heliostats in the field can be optimized.

Possible extensions for the implemented model could be:

- An aiming strategy should be used during optimization. It was shown above, that the flux distribution affects the receiver efficiency significantly so directly including a strategy into the model would lead to more reliable results.
- Discretize the sky and compute the optical efficiencies for the discretization nodes as proposed by Schöttl et al. [56]. This would make the costly optical simulation more efficient and it would be possible to implement a transient simulation that is fast enough for use in optimization.
- When implementing a transient simulation, the storage needs to be modeled in the sense that there is an actual storage filling strategy. With a storage model implemented, additional variables could be optimized, e.g., the storage capacity.

References

[1] Abengoa. About Atacama-1. Website. URL `http://www.abengoa.com/web/en/novedades/atacama-1/acerca/imagenes/`. Accessed November 1, 2017.

[2] K.G. Allen, T.W. von Backström, D.G. Kröger, and A.F.M. Kisters. Rock bed storage for solar thermal power plants: Rock characteristics, suitability, and availability. *Solar Energy Materials and Solar Cells*, 126:170–183, July 2014.

[3] Florian Arbes, Markus Wöhrbach, Daniel Gebreiter, and Gerhard Weinrebe. Towards high efficiency heliostat fields. In *Proceedings of the 22nd SolarPACES 2016 International Conference, Abu Dhabi, UAE*, volume 1850 of *AIP Conference Proceedings*. AIP Publishing, 2017.

[4] Thomas Ashley, Emilio Carrizosa, and Enrique Fernández-Cara. Optimisation of aiming strategies in solar power tower plants. *Energy*, 137:285–291, October 2017.

[5] Germain Augsburger. *Thermo-economic optimisation of large solar tower power plants*. PhD thesis, École Polytechnique Fédérale de Lausanne, 2013.

[6] Markus Balz, Verena Göcke, Thomas Keck, Finn von Reeken, Gerhard Weinrebe, and Markus Wöhrbach. Stellio–development, construction and testing of a smart heliostat. In Vikesh Rajpaul and Christoph Richter, editors, *Proceedings of the 21st SolarPACES International Conference (SolarPACES 2015)*, volume 1734 of *AIP Conference Proceedings*. AIP Publishing, 2016.

[7] Boris Belhomme, Robert Pitz-Paal, Peter Schwarzbözl, and Steffen Ulmer. A new fast ray tracing tool for high-precision simulation of heliostat fields. *Journal of Solar Energy Engineering*, 131(3), June 2009.

[8] M. Blanco, Juana M. Amieva, and Azael Mancilla. The tonatiuh software development project: An open source approach to the simulation of solar concentrating systems. *Proceedings of the IMEC2005, Orlando, FL*, pages 157–164, 2005.

[9] Juan Ignacio Burgaleta, Santiago Arias, and Diego Ramirez. Gemasolar, the first tower thermosolar commercial plant with molten salt storage. In *Proceedings of the SolarPACES 2011 Conference, Granada, Spain*, 2011.

[10] John Burkardt. Quadrature rules for the triangle. Open Source Software Library, 2014. URL `https://people.sc.fsu.edu/~jburkardt/cpp_src/triangle_dunavant_rule/triangle_dunavant_rule.html`. Last revised June 29, 2014.

[11] João P Cardoso, Amaia Mutuberria, Costas Marakkos, Peter Schöttl, Tiago Osório, and Iñigo Les. New functionalities for the tonatiuh ray-tracing software. In *Proceeding of the SolarPACES 2017 International Conference*, 2017.

[12] Joshua M. Christian and Clifford K. Ho. CFD simulation and heat loss analysis of the solar two power tower receiver. In *ASME 2012 6th International Conference on Energy Sustainability collocated with the ASME 2012 10th International Conference on Fuel Cell Science, Engineering and Technology*, pages 227–235. American Society of Mechanical Engineers, 2012.

[13] S.W. Churchill and M. Bernstein. A correlating equation for forced convection from gases and liquids to a circular cylinder in crossflow. *Journal of Heat Transfer*, 99(2):300–306, May 1977.

[14] Wikimedia Commons. Photographie d'un héliostat du site de Thémis. Online Resource. URL `https://commons.wikimedia.org/wiki/File:Heliostat.jpg`. Last modified May 19, 2009.

[15] Aalborg CSP. Solar tower receiver for superheated steam. Website. URL `http://www.aalborgcsp.dk/projects/concentrated-solar-power/solar-tower-receiver-for-superheated-steam.aspx`. Accessed October 28, 2017.

[16] Wolfgang Dahmen and Arnold Reusken. *Numerik für Ingenieure und Naturwissenschaftler*. Springer, 2nd edition, 2008. ISBN 978-3-540-76492-2.

[17] Shaozhong Deng. Math 5172 – Finite Element Method: Quadrature formulas in two dimensions. Lecture Notes Lecture 15, Dept. of Mathematics and Statistics, Univ. of North Carolina at Charlotte, 2010. URL `http://math2.uncc.edu/~shaodeng/TEACHING/math5172/Lectures/Lect_15.PDF`. Accessed August 1, 2017.

[18] Carmen-Ana Domínguez-Bravo. *Optimization Models in Solar Power Tower Plants Design: Design of the Heliostat Field and the Tower Receivers*. PhD thesis, Universidad de Sevilla, 2015.

[19] Carmen-Ana Domínguez-Bravo, Sebastian-James Bode, Gregor Heiming, Pascal Richter, Emilio Carrizosa, Enrique Fernández-Cara, Martin Frank, and Paul Gauché. Field-design optimization with triangular heliostat pods. In Vikesh Rajpaul and Christoph Richter, editors, *Proceedings of the 21st SolarPACES International Conference (SolarPACES 2015)*, volume 1734 of *AIP Conference Proceedings*. AIP Publishing, 2016.

[20] John A. Duffie and William A. Beckman. *Solar Engineering of Thermal Processes*. John Wiley & Sons, fourth edition, 2013. ISBN 978-0-470-87366-3.

[21] D.A. Dunavant. High degree efficient symmetrical gaussian quadrature rules for the triangle. *International Journal for Numerical Methods in Engineering*, 21: 1129–1148, 1985.

[22] ecoideaz. Concentrated solar power in india – still in infancy. Website. URL http://www.ecoideaz.com/expert-corner/concentrated-solar-power-in-india-still-in-infancy. Accessed November 14, 2017.

[23] Torresol Energy. Photo library. Website. URL http://www.torresolenergy.com/TORRESOL/image-library/en. Accessed November 14, 2017.

[24] Michael Epstein, D. Liebermann, M. Rosh, and Arthur J. Shor. Solar testing of 2 MW_{th} water/steam receiver at the weizmann institute solar tower. *Solar Energy Materials*, 24(1–4):265–278, December 1991.

[25] Robert Flesch, Cathy Frantz, Daniel Maldonado Quinto, and Schwarzbözl. Towards an optimal aiming for molten salt power towers. *Solar Energy*, 155:1273–1281, October 2017.

[26] Oliver Garbrecht. *Large Eddy Simulation of Three-dimensional Mixed Convection on a Vertical Plate*. PhD thesis, RWTH Aachen University, 2017.

[27] Paul Glassermann. *Monte Carlo Methods in Financial Engineering*, volume 53 of *Stochastic Modelling and Applied Probability*. Springer, 2003. ISBN 978-1-4419-1822-2.

[28] Volker Gnielinski. Neue gleichungen für den wärme- und den stoffübergang in turbulent durchströmten rohren und kanälen. *Forschung im Ingenieurwesen*, 41 (1):8–16, 1975.

[29] Google Inc. Google maps. Website. URL https://www.google.de/maps. Accessed November 11, 2017.

[30] Axel Grundmann and H.M. Moeller. Invariant integration formulas for the n-simplex by combinatorial methods. *SIAM Journal on Numerical Analysis*, 15(2): 282–290, April 1978.

[31] Gregor Heiming. SunFlower: A new solar tower simulation method for use in field layout optimization. Presentation at the SolarPACES 2017 International Conference, 2017.

[32] Klaus Hennecke, Peter Schwarzbözl, Bernhard Hoffschmidt, Joachim Göttsche, Gerrit Koll, Matthias Beuter, and Thomas Hartz. The solar power tower Jülich – a solar thermal power plant for test and demonstration of air receiver. In D. Yogi Goswami and Yuwen Zhao, editors, *Proceedings of ISES World Congress 2007 (Vol. I – Vol. V)*, pages 1749–1753. Springer, September 2007.

[33] R. Hilpert. Wärmeabgabe von geheizten Drähten und Rohren im Luftstrom. *Forschung auf dem Gebiete des Ingenieurwesens A*, 4(5):215–224, September 1933.

[34] Reinhold Kneer. Wärme- und Stoffübertragung I/II, Vorlesungsskript. Lecture notes, Lehrstuhl für Wärme- und Stoffübertragung, RWTH Aachen University, 2015. Ausgabe vom 2. September 2015.

[35] Gregory J. Kolb. Economic evaluation of solar-only and hybrid power towers using molten-salt technology. *Solar Energy*, 62(1):51–61, 1998.

[36] James N. Larmuth, Willem A. Landman, and Paul Gauché. A top-down approach to heliostat cost reduction. In Vikesh Rajpaul and Christoph Richter, editors, *Proceedings of the 21st SolarPACES International Conference (SolarPACES 2015)*, volume 1734 of *AIP Conference Proceedings*. AIP Publishing, 2016.

[37] Matti Lubkoll, Theodor W. von Backström, and Thomas M. Harms. Performance outlook of the SCRAP receiver. In Vikesh Rajpaul and Christoph Richter, editors, *Proceedings of the 21st SolarPACES International Conference (SolarPACES 2015)*, volume 1734 of *AIP Conference Proceedings*. AIP Publishing, 2016.

[38] S.L. Lutchman, A.A. Groenwold, P. Gauché, and S. Bode. On using a gradient-based method for heliostat field layout optimization. In *Proceedings of the SolarPACES 2013 International Conference*, volume 49 of *Energy Procedia*, pages 1429–1438. Elsevier, 2014.

[39] J.N. Lyness and D. Jespersen. Moderate degree symmetric quadrature rules for the triangle. *IMA Journal of Applied Mathematics*, 15(1):19–32, February 1975.

[40] Gabriel Morin. *Techno-Economic Design Optimization of Solar Thermal Power Plants*. PhD thesis, Technische Universität Braunschweig, 2011.

[41] National Renewable Energy Laboratory (NREL). SSC (SAM Simulation Core). Open Source Software Repository, 2017. URL `https://github.com/NREL/SSC`. Last modified October 20, 2017.

[42] Corey J. Noone, Manuel Torrilhon, and Alexander Mitsos. Heliostat field optimization: A new computationally efficient and biomimetic layout. *Solar Energy*, 86(2):792–803, February 2012.

[43] Franziska Ossenbrink. Shortest cable routing of heliostats in solar tower power plants. Bachelor's thesis, RWTH Aachen University, September 2017.

[44] Rafael Osuna, Valeric Fernandez, Manuel Romero, and M$^{\underline{a}}$ Jesus Marcos. PS10, a 10 MW solar tower power plant for southern spain. In *Energy 2000: The Beginning of a New Millennium*, pages 386–393. CRC Press, July 2000. ISBN 978-1587160165.

[45] James E. Pacheco, Robert W. Bradshaw, Daniel B. Dawson, Wilfredo De la Rosa, Rockwell Gilbert, Steven H. Goods, Mary Jane Hale, Peter Jacobs, Scott A. Jones, Gregory J. Kolb, Michael R. Prairie, Hugh E. Reilly, Steven K. Showalter, and

Lorin L. Vant-Hull. Final test and evaluation results from the solar two project. Technical Report SAND2002-0120, Sandia National Laboratories, Albuquerque, NM (USA), January 2002.

[46] PennEnergy. AREVA marks major milestone at concentrated solar power project. Website, 2013. URL `http://www.pennenergy.com/articles/pennenergy/2013/12/areva-marks-major-milestone-at-concentrated-solar-power-project.html`. Accessed November 14, 2017.

[47] B.S. Petukhov. Heat transfer and friction in turbulent pipe flow with variable physical properties. In James P Hartnett and Thomas F Irvine, editors, *Advances in Heat Transfer*, volume 6, pages 503–564. Elsevier, 1970.

[48] Pascal Richter. *Simulation and Optimization of Solar Thermal Power Plants*. PhD thesis, RWTH Aachen University, 2017.

[49] Pascal Richter, Martin Frank, and Erika Ábrahám. Multi-objective optimization of solar tower heliostat fields. In Giovanni Russo, Vincenzo Capasso, Giuseppe Nicosia, and Vittorio Romano, editors, *Progress in Industrial Mathematics at ECMI 2014*, volume 22 of *The European Consortium for Mathematics in Industry*, pages 771–778. Springer International Publishing, 2016. ISBN 978-3-319-23412-0.

[50] Pascal Richter, Gregor Heiming, Nils Lukas, and Martin Frank. SunFlower: A new solar tower simulation method for use in field layout optimization. In *Proceeding of the SolarPACES 2017 International Conference*, 2017.

[51] Marc Röger, Lars Amsbeck, Birgit Gobereit, and Reiner Buch. Face-down solid particle receiver using recirculation. *Journal of Solar Energy Engineering*, 133(3), July 2011.

[52] Marcelino Sánchez and Manuel Romero. Methodology for generation of heliostat field layout in central receiver systems based on yearly normalized energy surfaces. *Solar Energy*, 80(7):861–874, July 2006.

[53] Sargent & Lundy LLC Consulting Group. Assessment of parabolic trough and power tower solar technology cost and performance forecasts. Subcontractor Report NREL/SR-550-34440, National Renewable Energy Laboratory, Golden, CO (USA), October 2003.

[54] schlaich bergermann partner (sbp). Stellio Heliostat – the state-of-the-art Concentrating Solar Power (CSP). Website. URL `http://www.sbp.de/themenwelt/stellio-heliostat-the-state-of-the-art-concentrating-solar-power-csp/`. Last modified April 23, 2016.

[55] Mark Schmitz, Peter Schwarzbözl, Reiner Buck, and Robert Pitz-Paal. Assessment of the potential improvement due to multiple apertures in central receiver systems with secondary concentrators. *Solar Energy*, 80(1):111–120, January 2006.

[56] Peter Schöttl, Karolina Ordóñez Moreno, De Wet van Rooyen, Gregor Bern, and Peter Nitz. Novel sky discretization method for optical annual assessment of solar tower plants. *Solar Energy*, 138:36–46, 2016.

[57] SENER. Valle 1 and valle 2 parabolic through plants. Website. URL `http://www.poweroilandgas.sener/gallery-multimedia`. Accessed November 13, 2017.

[58] Dennis L. Siebers and John S. Kraabel. Estimating convective energy losses from solar central receivers. Technical Report SAND84-8717, Sandia National Laboratories, Livermore, CA (USA), 1984.

[59] D.L. Siebers, R.F. Moffatt, and R.G. Schwind. Experimental, variable properties natural convection from a large, vertical, flat surface. *Journal of Heat Transfer*, 107(1):124–132, February 1985.

[60] Solargis. World solar resource maps. Website. URL `http://solargis.com/products/maps-and-gis-data/free/download/world`. Accessed November 4, 2017.

[61] SolarReserve. Crescent dunes. Website. URL `http://www.solarreserve.com/en/global-projects/csp/crescent-dunes`. Accessed November 3, 2017.

[62] Solar Thermal Energy Research Group (STERG). Technical Tour: SolarPACES 2015. Website. URL `http://sterg.sun.ac.za/solarpaces2015_tour/`. Accessed November 1, 2017.

[63] William B. Stine and Michael Geyer. *Power From The Sun*. online version, 2001. URL `http://www.powerfromthesun.net/book.html`. Accessed June 28, 2017.

[64] Arthur H. Stroud and Don Secrest. *Gaussian quadrature formulas*. Series in Automatic Computation. Prentice Hall, 1966.

[65] Ralf Uhlig, Cathy Frantz, and Andreas Fritsch. Effects of vertically ribbed surface roughness on the forced convective heat losses in central receiver systems. In Vikesh Rajpaul and Christoph Richter, editors, *Proceedings of the 21st SolarPACES International Conference (SolarPACES 2015)*, volume 1734 of *AIP Conference Proceedings*. AIP Publishing, 2016.

[66] Michael J. Wagner. Simulation and predictive performance modeling of utility-scale central receiver system power plants. Master's thesis, University of Wisconsin – Madison, 2008.

[67] S. Wandzura and H. Xiao. Symmetric quadrature rules on a triangle. *Computers & Mathematics with Applications*, 45(12):1829–1840, June 2003.

[68] Basin & Range Watch. Crescent Dunes Solar Energy Project. Website. URL `http://www.basinandrangewatch.org/CrescentDune.html`. Accessed June 13, 2017.

[69] Tim Wendelin. SolTRACE: A new optical modeling tool for concentrating solar optics. In *ASME 2003 International Solar Energy Conference*, pages 253–260. American Society of Mechanical Engineers, 2003.

[70] Tim Wendelin, Aron Dobos, and Allan Lewandowski. SolTrace: A ray-tracing code for complex solar optical systems. Technical Report NREL/TP-5500-59163, National Renewable Energy Laboratory (NREL), Golden, CO (USA), October 2013.

[71] Stephen Whitaker. Forced convection heat transfer correlations for flow in pipes, past flat plates, single cylinders, single spheres, and for flow in packed beds and tube bundles. *AIChE Journal*, 18(2):361–371, March 1972.

[72] C-J Winter, Rudolf L Sizmann, and Lorin L Vant-Hull, editors. *Solar Power Plants – Fundamentals, Technology, Systems, Economics*. Springer-Verlag Berlin, Heidelberg, 1991. ISBN 978-3-642-64759-8.

[73] R. Zanino, R. Bonifetto, J.M. Christian, C.K. Ho, and L. Savoldi Richard. Effects of RANS-type turbulence models on the convective heat loss computed by CFD in the solar two power tower. In *Proceedings of the SolarPACES 2013 International Conference*, volume 49 of *Energy Procedia*, pages 569–578. Elsevier, 2014.